



**HAL**  
open science

# Multiscalar DIC Analyses of Granular String Under Stretch Reveal Non-standard Deformation Mechanisms

Nima Nejadsadeghi, Michele de Angelo, Anil Misra, François Hild

► **To cite this version:**

Nima Nejadsadeghi, Michele de Angelo, Anil Misra, François Hild. Multiscalar DIC Analyses of Granular String Under Stretch Reveal Non-standard Deformation Mechanisms. *International Journal of Solids and Structures*, 2022, 239-240, pp.111402. 10.1016/j.ijsolstr.2021.111402 . hal-03482296

**HAL Id: hal-03482296**

**<https://hal.science/hal-03482296v1>**

Submitted on 15 Dec 2021

**HAL** is a multi-disciplinary open access archive for the deposit and dissemination of scientific research documents, whether they are published or not. The documents may come from teaching and research institutions in France or abroad, or from public or private research centers.

L'archive ouverte pluridisciplinaire **HAL**, est destinée au dépôt et à la diffusion de documents scientifiques de niveau recherche, publiés ou non, émanant des établissements d'enseignement et de recherche français ou étrangers, des laboratoires publics ou privés.

1 Highlights

2 **Multiscalar DIC Analyses of Granular String Under Stretch Reveal Non-standard Deforma-**  
3 **tion Mechanisms**

4 Nima Nejadsadeghi, Michele De Angelo, Anil Misra, François Hild

- 5 ● DIC analyses with a suite of multiscalar kinematic assumptions are applied to measure dis-  
6 placement fields in a grain-string under extension
- 7 ● Analyses reveal non-standard deformation mechanisms that underlie the emergent macroscale  
8 response
- 9 ● Multiscale DIC analyses can elucidate otherwise latent mechanisms that indicate the need  
10 for refined kinematic descriptions

# Multiscalar DIC Analyses of Granular String Under Stretch Reveal Non-standard Deformation Mechanisms

Nima Nejadi Sadeghi<sup>a</sup>, Michele De Angelo<sup>b,c</sup>, Anil Misra<sup>a,b</sup> and François Hild<sup>d,\*</sup>

<sup>a</sup>Mechanical Engineering Department, University of Kansas, 1530 W 15th Street, Learned Hall, Lawrence, KS 66047-7609, USA

<sup>b</sup>Civil, Environmental and Architectural Engineering Department, University of Kansas, 1530 W 15th Street, Learned Hall, Lawrence, KS 66047-7609, USA

<sup>c</sup>Dipartimento di Ingegneria Civile, Edile-Architettura e Ambientale, Università degli Studi dell'Aquila, Via Giovanni Gronchi 18 - Zona industriale di Pile, 67100 L'Aquila, Italy

<sup>d</sup>Université Paris-Saclay, ENS Paris-Saclay, CNRS, LMT - Laboratoire de Mécanique et Technologie, 4 avenue des sciences, 91190 Gif-sur-Yvette, France

## ARTICLE INFO

*Keywords:*

Chirality

Digital Image correlation (DIC)

Granular material


Microstructured solid

Metamaterial

## ABSTRACT

Mechanical tests designed to measure classical behavior do not provide information underlying the macroscale response. Multiscalar digital image correlation (DIC) can be employed in these experiments to expose the micro-mechanisms that lead to the emergent macroscale behavior. A multiscalar DIC methodology is applied to study the extensional behavior of a particular granular string with chiral properties. DIC was performed at macroscale in which the underlying microstructure is overlooked and the construct is treated as a continuum bar. Further, the underlying microstructure was exploited in a microscale DIC analysis to expose the rich deformation regimes. In addition, mesoscale analysis was carried out to extract the rigid body motions that characterize a granular material system. These analyses were performed for two types of surface patterns and measurement uncertainties were quantified. The microscale results show that the grain string can be treated as a granular material composed of a set of nearly rigid grains that store elastic energy through intergranular mechanisms. Further, the results reveal non-standard deformation mechanisms that underlie the chiral granular string subjected to extension. These mechanisms include grain rotations that are coherent as opposed to gear-like grain rotation. More notably, grain transverse displacements are observed that are controlled by the behavior of the grain interconnections.

\*Corresponding author.

 francois.hild@ens-paris-saclay.fr (F. Hild); francois.hild@ens-paris-saclay.fr (F. Hild)

ORCID(s): 0000-0002-2890-6483 (N. Nejadi Sadeghi); 0000-0002-4216-7525 (M. De Angelo);

0000-0002-9761-2358 (A. Misra); 0000-0001-5553-0066 (F. Hild)

## 45 **1. Introduction**

46 Emergent response at the macroscale not only depends upon the microstructure, but also the mi-  
47 cromechanics of interactions between micro-units. In many materials, these micromechanisms are  
48 latent and are not easily discoverable. To illustrate this phenomena, a granular microstructure was  
49 designed. This structure consists of a string of connected grains, whose connections are endowed  
50 with a particular behavior that couples tangential and normal grain-pair responses (Giorgio et al.,  
51 2020; Misra et al., 2020), thereby resulting in a chiral behavior that is not invariant to coordinate  
52 inversion. In other words, the mirror image of the geometry cannot be mapped onto itself by mere  
53 translations and rotations. The dynamics of chiral lattices has extensively been studied in the litera-  
54 ture due to their peculiar phononic properties. In contradistinction to the chirality observed in wave  
55 transmission, as in optics, static deformation of solids may also exhibit a chiral behavior. A number  
56 of works have described chiral behaviors of lattice-like constructs by direct simulation of the mi-  
57 crostructures using classical continuum theories (Alderson et al., 2010; Dirrenberger et al., 2011).  
58 On the other hand, experimental results have suggested the use of generalized continuum theories  
59 to correctly predict chirality. This observation has led several researchers to describe the complex  
60 deformation of chiral materials adopting generalized continuum theories (*e.g.*, see (Spadoni et al.,  
61 2009; Liu et al., 2011, 2012; Chen et al., 2014; Frenzel et al., 2017; Duan et al., 2018; Poncelet  
62 et al., 2018; Reasa and Lakes, 2019; Wu et al., 2019; Biswas et al., 2020; Chen et al., 2020) to name  
63 a few).

64 In this work, the studied granular string design was inspired by micromorphic models of gran-  
65 ular materials based upon granular micromechanics (Nejadsadeghi and Misra, 2020). Metamate-  
66 rials, whose behavior is expected to be tailored to achieve some desired function, can benefit from  
67 rational design approach based upon predictive theories (dell'Isola et al., 2020). In this regard, the  
68 recent design and fabrication of pantographic metamaterials based upon higher gradient theories,  
69 and chiral granular materials are exemplar of such rational design (dell'Isola et al., 2019; Misra  
70 et al., 2020). These recent works have shown that theoretical methods using approaches such as

71 generalized continuum theories offer efficient ways for rational design of metamaterials (as op-  
72 posed to trial and error or other *ad hoc* approaches, see for example the reviews by Surjadi et al.  
73 (2019); Barchiesi et al. (2019)). These methods have the ability to describe how to harness stored  
74 elastic energy in internal deformation modes, including second and higher gradients modes (Al-  
75 ibert et al., 2003; Nejadi Sadeghi and Misra, 2020), grain rotations/spins (Poorsolhjouy and Misra,  
76 2019), and non-standard coupling of shear and rotations (De Angelo et al., 2020; Barchiesi et al.,  
77 2021). As a consequence, these theories predict not only the emergent behavior at the macroscale,  
78 such as negative Poisson's effect, chirality, inherent anisotropy, varying Poynting effects (Misra  
79 et al., 2018; Auger et al., 2021) and couplings between different macrophenomena (Poncelet et al.,  
80 2018), but also their microscale origins. In the latter study, digital image correlation (DIC) was  
81 useful in allowing the authors to prove the breakdown of Cauchy elasticity in the analysis of non-  
82 centro-symmetric lattices.

83 The significance of grain-scale measurements has been recognized early in granular mechan-  
84 ics (Drescher and de Josselin de Jong, 1972) using the so-called "Schneebeli material" (Schneebeli,  
85 1956). Among the earliest measurements of the grain rigid body kinematics in deforming granular  
86 packs incorporating grain displacements and rotations was that reported in 1997 (Misra and Jiang,  
87 1997). More recently, DIC, which was originally introduced to measure the deformation of con-  
88 tinuum media (Sutton, 2013), has also been considered when seeking kinematic fields in granular  
89 materials. DIC was used to quantify shear band formation and growth in sands (Rechenmacher,  
90 2006). The author used a commercial code without accounting for the discrete behavior of grains.  
91 Similarly, Hall et al. (2010) implemented subset-based DIC, which was not adapted to the underly-  
92 ing grains, to study localization phenomena in granular materials. Larsson et al. (2020) measured  
93 the flow of granular materials for validation purposes of a discrete model. Conversely, Richefeu  
94 et al. (2012); Richefeu and Combe (2020) tracked the rigid body motions of individual grains with  
95 square and other shaped domains inside each grain to study shear experiments. Further, Bruno  
96 et al. (2016) used a similar approach to analyze a Flamant experiment on a granular material.

97 Multiscale DIC can be implemented to reveal micromechanisms that may not be clearly iden-  
98 tified in mechanical tests. For example, the recent work on multiscale DIC application to panto-  
99 graphic structures has revealed additional relative shear deformation modes at the hinges besides  
100 providing a detailed kinematic description of fiber bending (Hild et al., 2021). In the present paper,  
101 a similar type of multiscale analyses is performed on chiral granular strings subjected to extension.  
102 The granular string sample in which the grains were interconnected using a particular “duoske-  
103 lion” bridge was 3D printed. Two different surface preparations for DIC were applied on the two  
104 opposite surfaces of the specimen. The specimen was then subjected to two sequential extension  
105 tests, and images acquired at different loading steps for each surface. DIC analyses were then per-  
106 formed at 3 scales: i) macroscale, in which the granular string was treated as a continuum bar; ii)  
107 microscale, in which all the detailed microstructural characteristics were fully represented; and iii)  
108 mesoscale in which the effort was devoted to obtaining rigid body motions pertinent to granular  
109 material systems. Uncertainties associated with the DIC results were analyzed and quantified. The  
110 results of DIC at the 3 spatial scales were described with particular attention to the non-standard  
111 deformations mechanisms revealed through such analyses.

## 112 **2. Sample and Experiment**

### 113 **2.1. Sample Preparation**

114 The prototypical granular string made of 11 grains connected via the conceived connection  
115 was rendered using the CAD software SolidWorks (Dassault Systems SolidWorks Corporation,  
116 Waltham, MA, USA). The 11-grain string is terminated at both ends with a flat extension designed  
117 for gripping the specimen in the testing machine. The dimensions of the features comprising the  
118 1D granular string are given in Figure 1 for the specimen discussed in this paper. The out-of-plane  
119 thickness of the granular string was specified to be 4 mm so as to prevent warpage of the sample  
120 in the fabrication process, while also admitting a 2D planar analysis of deformations (Figure 2(a)).  
121 The CAD model was fabricated using a “Durable Resin” monomer in the Form 3 3D printer (Form-  
122 Labs, USA). The Form 3 3D printer is based upon Low Force Stereolithography (LFS)<sup>TM</sup>, which

123 photo-polymerizes the resin into the desired shape. The  $XY$  resolution and layer thickness was  
 124  $\approx 50 \mu\text{m}$  such that sub-millimeter features were achieved with good precision.



Geometrical parameter	Dimension (mm)
$l$	$10.5 \pm 0.1$
$r$	$2.5 \pm 0.1$
$t$	$0.6 \pm 0.1$
$b$	$1.0 \pm 0.1$

**Figure 1:** Geometrical parameters corresponding to the proposed grain-pair interaction model

## 125 2.2. Experiment

126 The fabricated granular string was tested under extension in an ElectroForce 3200 (TA Instru-  
 127 ments) mechanical testing machine equipped with a load cell of capacity  $\pm 450 \text{ N}$ , a measurement  
 128 uncertainty of 0.1% and precision of 0.001 N, and a displacement transducer with a range  $\pm 6.5 \text{ mm}$ ,  
 129 a measurement uncertainty of 0.1% and precision 0.001 mm. Figure 2(b) shows the experimental  
 130 setup indicating the clamped boundary conditions, such that on the top grain of the string a vertical  
 131 displacement is applied while the lateral displacement and rotations are constrained, and on the  
 132 bottom grain both the vertical and lateral displacements as well as the rotations are constrained.  
 133 The granular string was stretched at a rate of 0.2 mm/s up to a total extension of 10 mm.

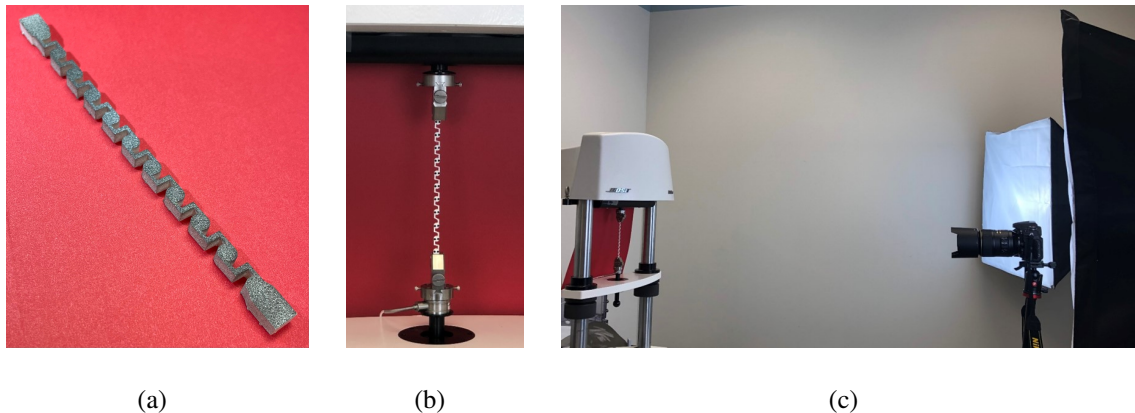


**Figure 2:** (a) Speckled sample surface. Experimental (b) and picture acquisition (c) setup

134 Table 1 lists the hardware parameters of the optical setup. To facilitate data extraction from  
 135 images, a white background was used in the case of dotted pattern, while a red background was  
 136 adopted in the case of speckle pattern. For the purpose of image acquisition in both cases, soft  
 137 boxes were used to generate diffuse lighting (Figure 2(c)).

**Table 1**

DIC hardware parameters

Camera	NIKON D300
Definition	4288 × 2848 pixels (RGB image)
Gray Levels amplitude	8 bits
Lens	AF-S VR Micro-Nikkor 105mm f/2.8G ED
Aperture	$f/4.5$
Field of view	111 × 74 mm <sup>2</sup>
Image scale	60 μm/px (B&W image)
Stand-off distance	≈ 90 cm
Image acquisition rate	1/5-1/3 fps
Exposure time	20 ms
Patterning technique	Sprayed black paint or black dots
Pattern feature size	3 px (speckle pattern) or 31 px (dots)

138 The extension experiment was repeated twice for the same specimen to acquire images for  
 139 the two surface patterns. In the first case, two dots were manually drawn on each grain surface  
 140 (Appendix A). In the second case, a speckle pattern was spray painted upon the surface. While the  
 141 dotted pattern is a legacy approach to determine the rigid body motion of the grains (Appendix A),  
 142 the speckle pattern was expected to provide a richer outcome of kinematics at various spatial scales,  
 143 and detailed deformation behavior of the connections. Figure 3 gives the initial (*i.e.*, undeformed)  
 144 configuration and all deformed configurations under step-wise extension of the speckled surface.



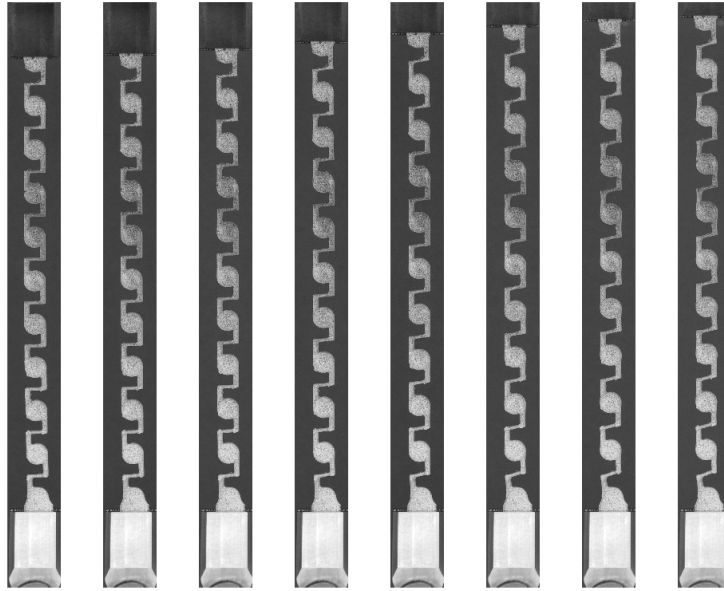


**Figure 3:** Cropped gray level images of the extensional test with speckled grains

### 145 3. Multiscale DIC Strategies

146 With the aim of illustrating the role of micromechanisms, and power of DIC in extracting the  
 147 details of the deformation behavior, the elongation experiment was analyzed at multiple spatial  
 148 scales using a suite of different kinematic assumptions. To this end, the granular string may be  
 149 represented in 3 different ways: i) as a continuous bar devoid of structure when the observation is  
 150 at a coarse or the macroscale; ii) as a structured bar in which the geometrical features, such as beam-  
 151 like elements connecting bulky circular grains, are observable, defined here as the microscale; and  
 152 iii) as a set of rigid interconnected grains whose deformation can be represented by following the  
 153 grain motions, defined as the mesoscale.

#### 154 3.1. Kinematic Bases

155 For macroscale analyses, the grain-string structure is taken as a continuum bar of homogeneous  
 156 cross-section, such that no distinction was made between the solid phase and surrounding air. The  
 157 macroscale assumption was deemed to represent a very small finite volume element of a large body  
 158 analyzed at a scale in which the grains were indistinguishable. Finite element discretizations of the

159 assumed bar were considered with 3-noded triangular (T3) elements. The only requirement was  
160 that the structured meshes encompass the whole solid phase (Figures 5 and 16). Modeling of the  
161 behavior of granular materials that emerges at the macroscale are known to be challenging due  
162 to the effects of micromechanisms. An analysis at the macroscale without direct representation  
163 of the microstructure could aid in revealing these emergent effects. Such results could be useful  
164 for evaluation of macroscopic continuum models developed to describe the deformation of such  
165 granular materials (Rechenmacher, 2006; Vardoulakis, 2019; Larsson et al., 2020). An alternative  
166 application, and one that is particularly useful for the multiscalar efforts described here, is to uti-  
167 lize the macroscale result to initialize more refined DIC analyses with the measured displacement  
168 field at the macroscale. Such strategy was used herein and enabled the number of iterations to be  
169 significantly lowered for the microscale and mesoscale analyses.

170 Discrete models of granular materials have been formulated in terms of rigid body motions of  
171 the grains given that the deformations are often localized in very small regions where the grains  
172 connect with each other (see, for example, the widely used discrete element models (Cundall and  
173 Strack, 1979; Jean and Moreau, 1987; Holtzman et al., 2010)). Irrespective of the deformation lo-  
174 cation, the discrete view that considers grain-displacements and grain-rotation about their barycen-  
175 ters, presents an effective model for describing the collective deformation of large collections of  
176 deformable grains (Turco et al., 2019). Therefore, the determination of the grain motions is of wide  
177 interest both from the viewpoint of validation of discrete models as well as for the development  
178 of plausible grain-interactions relationships relevant to these models as well as those that aim to  
179 link grain-scale to macroscale continua (Nejadsadeghi and Misra, 2020). From the discrete model  
180 (defined here as the mesoscale) viewpoint, the deformation of the string can be represented by  
181 following the motions of the set of grains.

182 In this work, mesoscale analyses were performed in two ways. First, mesoscale analyses (*i.e.*, at  
183 the scale of each grain) were conducted with 3 degrees of freedom (DOFs) per grain (*i.e.*, in-plane  
184 translations of the grain center, and corresponding rigid body rotation) for both surface prepa-

185 rations. In all these cases, circular regions of interest (ROIs) were considered. Second, for the  
186 speckled surface, 6 DOFs per grain were also analyzed (*i.e.*, in-plane translations of the grain cen-  
187 ter, and corresponding mean in-plane deformation gradient). The 6 DOFs analysis was feasible for  
188 the speckled surface due to the availability of information over the whole grain surface as opposed  
189 to the case of dotted surface. Such an analysis can aid in validating the mesoscale treatment of the  
190 granular string using a discrete model by evaluating the state of deformation within the grain.

191 At the microscale of the granular string, the deformation was analyzed for the detailed geo-  
192 metrical structure for the speckled surface. A preliminary step was required to construct meshes  
193 that were consistent with the underlying mesostructure (Figures 4(left) and 18(right)). To this end,  
194 a so-called backtracking procedure was utilized (dell’Isola et al., 2019; Hild et al., 2021). From  
195 the knowledge of the nominal geometry, a mask was created (Figure 4(center)) and a mesh was  
196 generated using Gmsh (Geuzaine and Remacle, 2009). The two images were then registered via  
197 regularized DIC with an auxiliary mesh corresponding to the first discretization at the macroscale  
198 (Figure 5(left)). At the end of the procedure, the mesh was backtracked by using the measured  
199 displacement field (Figure 4(right)). This operation was also applied to the center of each grain  
200 that was initially determined in the nominal configuration. For the dotted surface, discrete analyses  
201 were performed in which 4 T3 elements were considered with one node for each element coinci-  
202 dent with the dot center (Figure 18). Microscale analyses are particularly useful for understanding  
203 the behavior of grain interconnections. Needless to say, the microscale analysis is limited by the  
204 resolution of the image and may not reveal all the details of the interconnection deformation. How-  
205 ever, the intent in this particular work was not resolve how every element of the interconnections  
206 deformed but to reveal which aspect of the interconnections underwent the deformation. The aim  
207 of this analysis was to understand how the geometry of the interconnections could be modified to  
208 modulate the behavior of the overall system.

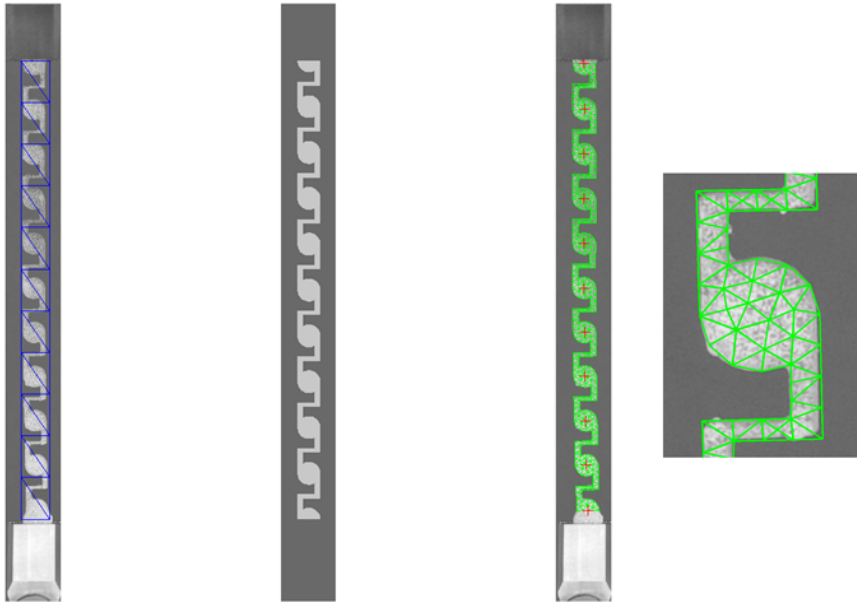


**Figure 4:** Backtracked mesh for microscale DIC of the speckled surface. The image of the reference configuration (left) was registered with that of the nominal configuration (middle) using the auxiliary mesh shown in blue. The backtracked mesh was laid over the reference image (right). Mesh details are shown for one of the grains. The grain centers (red crosses) are also depicted

209 For the results described in this paper, the DIC analyses were performed using the Correli 3.0  
 210 framework (Leclerc et al., 2015) in which Hencky-elastic regularization was implemented (Ta-  
 211 ble 2). The DIC framework followed herein is summarized in Appendix B.

Table 2

DIC analysis parameters

DIC software	Correli 3.0 (Leclerc et al., 2015)
Image filtering	none
Element length (mean)	see text
Shape functions	linear (T3)
Mesh	see Figures 5, 16, 4 and 18
Matching criterion	penalized sum of squared differences
Regularization length	100 px
Grain radius	50 px
Shape functions	3 or 6 (see text)
Matching criterion	sum of squared differences
Interpolant	cubic
Displacement noise-floor	see Table 3

### 212 3.2. Uncertainty Quantification

213 The displacement noise-floor is an important information for assessing the performance of the  
 214 selected DIC routine (iDICs et al., 2018; ASD-STAN prEN 4861 P1, 2018). In the present case,  
 215 there was only one image of the reference configuration. Fortunately, the sample structure cov-  
 216 ered a considerably small region in comparison to the full definition of the images. Consequently,  
 217 there were a large number of pixels in the background that did not cover the structures of interest.  
 218 Assuming that the camera remained stationary during the experiment as per the experimental pro-  
 219 tocol, it was possible to crop a large ROI of the background from all the images. All independent  
 220 ROI differences were computed and acquisition noise was estimated from the average variance of  
 221 each pixel of the ROI. The square root of the variance is then equal to  $\sqrt{2}\sigma$ , where  $\sigma$  denotes the  
 222 standard deviation of acquisition noise corrupting *each* image. For the two experiments reported  
 223 in this work, the lighting conditions and backgrounds were not identical. As expected, the stan-

224 dard deviations  $\sigma$  were different as well, namely, for the dotted surface  $\sqrt{2}\sigma = 1.2$  gray level, and  
225  $\sqrt{2}\sigma = 2.4$  gray levels for the speckle pattern.

226 Using the above estimate of acquisition noise, uncertainty quantification was performed by  
227 generating a series of 100 pictures in which Gaussian white noise was added with a standard de-  
228 viation of  $\sqrt{2}\sigma$  to the image of the reference configuration. DIC analyses were then run on these  
229 image series. The temporal standard deviation was then evaluated for each DOF  $v_i$  considered in  
230 the DIC analysis (Appendix B). For finite element discretizations, the mean variance was assessed  
231 per direction, and then its square root was obtained to assess the standard displacement uncertainty.

232 Table 3 gathers the results of this uncertainty quantification. Since one of the surfaces had only  
233 dots with no speckle pattern, the regularization length was increased to enable for a good conver-  
234 gence of DIC analyses. In the present case,  $\ell_{reg} = 100$  px for all meshes. Because the regularization  
235 length was greater than the element sizes considered herein, the uncertainties were controlled by  
236 the former. No dependence on mesh size was observed for both macroscale and microscale analy-  
237 ses. In addition, very low levels of uncertainties were achieved. In contrast, the discrete analyses  
238 around each black dot concerned very small areas for which the standard displacement uncertainty  
239 increased in comparison to continuous meshes. Last, for the analyses at the grain level with 3 or 6  
240 DOFs led to displacement uncertainties of the same order of magnitude than those observed with  
241 continuous meshes. The standard uncertainty levels for the last degrees of freedom referring to the  
242 rotation or the deformation gradient were rather small. This is due to the fact that the grain radius  
243 was equal to 50 px.

**Table 3**

Standard uncertainties of each DOF for the analyses at three different scales and for the two surface preparations. See text for the description of the kinematics associated with 3 and 6 DOFs

DIC analysis	Speckle	Dots
Macroscopic scale	0.004 px   0.004 px	0.004 px   0.003 px
Microscopic scale	0.007 px   0.007 px	0.010 px   0.008 px
Discrete	--	0.013 px   0.013 px
3 DOFs	0.003 px   0.003 px   $9 \times 10^{-5}$	0.002 px   0.002 px   $6 \times 10^{-5}$
6 DOFS	0.003 px   0.003 px   $1.1 \times 10^{-4}$	--

#### 244 **4. Probing the Three Different Kinematic Descriptions**

245 The gray level residuals are first analyzed as a way of probing the three kinematic bases before  
 246 discussing the findings from the DIC results. The applicability of the proposed multiscalar regis-  
 247 trations is evaluated by investigating the evolution of gray level residuals as the loading progresses  
 248 for each of the three kinematic bases. The gray level residuals indicate the suitability of each basis.

##### 249 **4.1. Macroscale analyses**

250 Figure 5 shows the three meshes considered for the macroscale analyses. To characterize the  
 251 mesh density, the element size was defined as the square root of the mean element surface. For the  
 252 speckled surface (Figure 5), the three element sizes were 79, 39, and 22 px, respectively. These  
 253 meshes were used to perform a convergence analysis by running DIC analyses with each mesh on  
 254 the image series. Two sets of results are reported. First, so called incremental DIC was conducted  
 255 in which the reference configuration of a new calculation corresponds to the previous deformed  
 256 configuration. This is possible since the mesh was gradually deformed according to the measured  
 257 incremental displacement. Such analysis enables very large displacement amplitudes to be mea-  
 258 sured, and the Lagrangian displacements are obtained by adding all incremental contributions.  
 259 However, it leads to an accumulation of DIC measurement errors. Once this first analysis was

260 completed, a second one (referred to as direct) was carried out in which the reference picture was  
 261 always the initial one, and the initial guess for any time step was that provided by the incremental  
 262 procedure. In the following, RMS residuals  $\rho_c$  (see Appendix B) are analyzed for any mesh and  
 263 both DIC routes.



**Figure 5:** Three meshes used for the DIC analyses at the macroscale of the speckled surface

264 Figure 6 shows the RMS residuals for the 7 analyzed pictures of the speckled surface with the  
 265 three different meshes. For the coarsest mesh (Figure 6(a)), no significant gain is observed when  
 266 direct and incremental analyses were performed. A small decrease is observed when finer meshes  
 267 were selected (Figure 6(b-c)). As the meshes were refined, the RMS residuals decreased a bit.  
 268 However, they could not be significantly lowered. This is due to the fact that the regularization  
 269 length was larger than the element size of any of the considered meshes. Last, it is worth noting  
 270 that the RMS residuals are significantly larger (*i.e.*, between 2 and 7 times) than the level associated  
 271 with acquisition noise (*i.e.*, 2.4 gray levels in the present case). Further, they degrade as the applied  
 272 displacement amplitude increased. This trend is not a shortcoming of the registration procedure  
 273 itself but is rather related to the fact that the selected kinematic basis was no longer able to fully



274 capture the details of the deformations at the microstructural level.

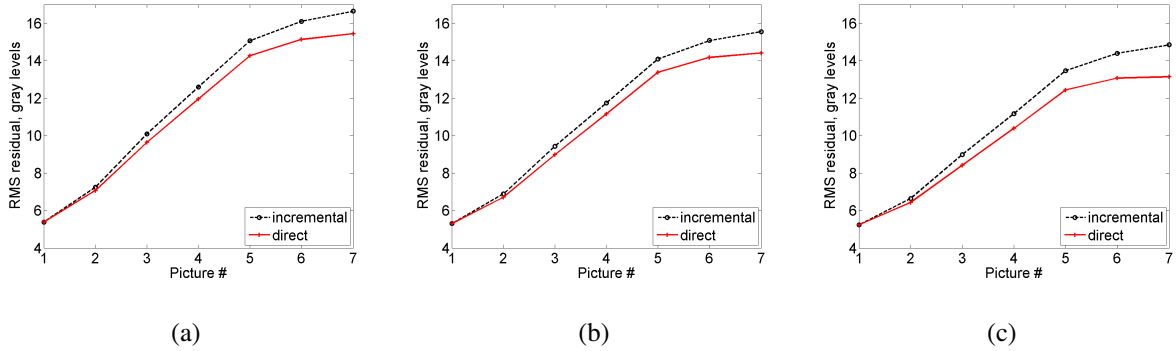


**Figure 6:** RMS gray level residuals for the three meshes of the speckled surface (Figure 5) and the two DIC routes

275 From the convergence analysis, it is concluded that any of the selected meshes is able to give  
 276 acceptable results for initialization purposes. No significant gain was observed when refining the  
 277 discretization because of the large regularization *and* the fact that the geometry was not adapted to  
 278 the underlying microstructure. This observation also applies to the results obtained with the dotted  
 279 surface (Figure 17).

#### 280 4.2. Mesoscale analyses

281 The following analyses were performed to extract the kinematic information at the grain-scale.  
 282 Circular ROIs were considered for each grain and DIC analyses were run independently. For each  
 283 grain, 3 DOFs were considered (*i.e.*, 2 rigid body translations and 1 rigid body rotation). Figure 7(a)  
 284 shows the change of RMS residuals for each grain and each image of the considered series. The  
 285 RMS residuals vary from 1 to less than 2 times the level associated with acquisition noise, which  
 286 is very low. These results prove that the selected kinematic basis is able to capture very well the  
 287 underlying motions of grains.

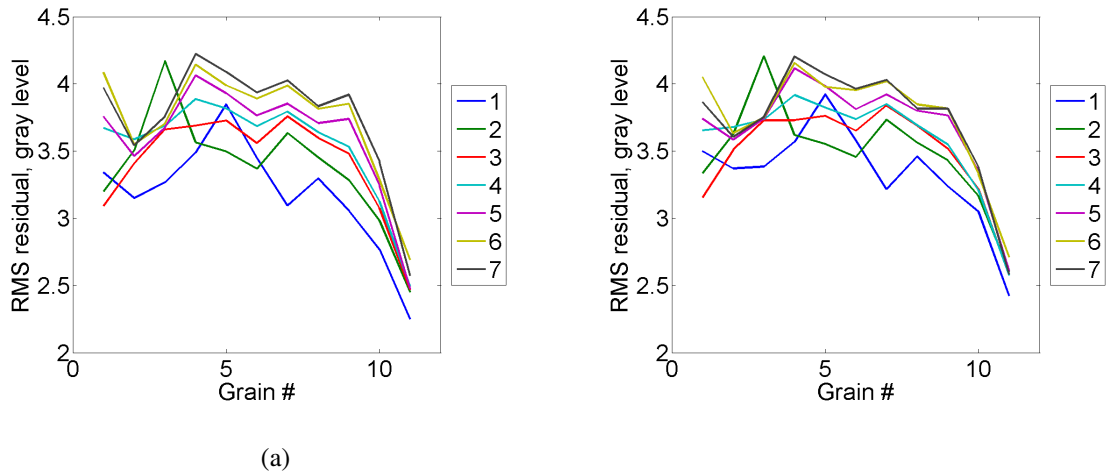
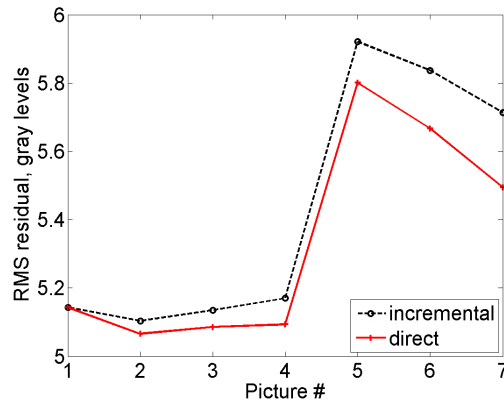


**Figure 7:** RMS gray level residuals for the DIC analyses with 3 DOFs (a) and six DOFs (b) per grain of the speckled surface (each line corresponds to one picture of the series)

288 To verify the assumption that the bulk of the grain suffered indistinguishable deformation, an  
 289 additional analysis was performed by allowing for uniform strains at the grain-scale (*i.e.*, defining  
 290 the kinematics using 6 DOFs instead of 3 for the rigid body motions). The RMS residuals for the 3-  
 291 DOF solution (Figure 7(a)) and with 6 DOFs (Figure 7(b)) show insignificant differences, proving  
 292 that the analyses with 3 DOFs were sufficient to capture the overall motions of each grain. It is  
 293 concluded that the bulk of the grain does not experience strain and the grain movement is governed  
 294 by the deformation at the connections between grain-pairs.

### 295 4.3. Microscale analyses

296 In the present case, the mean element size was equal to 16 px. Contrary to the macroscale  
 297 analyses, the RMS residuals did not vary significantly with the applied displacement (Figure 8).  
 298 Their average was of the order of 2.3 times the level due to acquisition noise. It is concluded that the  
 299 kinematics was very well captured by such analyses. If deformation details were to be sought, then  
 300 the mesh should be further refined (see Section 5.3), which is possible thanks to the regularization  
 301 strategy used herein.



(a)

**Figure 8:** RMS gray level residuals for the DIC analyses at the microscale of the speckled surface

302 This first series of results show that the macroscopic kinematics could be captured. However,  
 303 the degradation of the gray level residuals indicate that such description is not able to fully account  
 304 for local details of the deformation mechanisms of the granular string. For the grains themselves,  
 305 the hypothesis of rigid body motions was validated for any applied displacement amplitude. Last,  
 306 the analysis at the microscale was shown to be feasible thanks to the mesh that was tailored to the  
 307 underlying morphology of the granular string and its interconnections, in addition to the regular-  
 308 ization scheme based on Hencky elasticity.

## 309 5. Results for the Speckled Surface

310 The DIC results obtained from the analyses at different scales are now further commented for the  
 311 case of speckled surface. The discussion here focuses upon the deformation mechanisms revealed  
 312 through the multiscalar analysis. Similar results are obtained for the case of dotted surface and are  
 313 discussed in Appendix A.

### 314 5.1. Macroscale Analysis

315 Figure 9 gives the results of the direct analysis for the finest discretization and the final image  
 316 of the extension test (*i.e.*, the image at maximum applied displacement). Given that the maximum  
 317 displacement amplitude (*i.e.*, 180 px) was quite large, and the total number of images was few

318 (*i.e.*, 7 in the present case), the incremental analysis was the only one able to capture such large  
319 displacement increments, and was very useful to initialize subsequent direct DIC analyses.

320 The underlying geometry of the granular string expresses itself in the transverse displacement  
321 field (Figure 9(left)) in which a fluctuating pattern of positive and negative transverse displace-  
322 ments is observed. On the other hand, the longitudinal displacement field (Figure 9(middle)) shows  
323 a nominally monotonically varying trend. To explicate any fluctuating pattern in the longitudinal  
324 field, the mean strain component was deducted from the measured field. Displacement fluctua-  
325 tions are now observed in Figure 9(right), whose overall pattern is similar to that observed for the  
326 transverse component. These fluctuations (or deviations) from the erstwhile linear field is a charac-  
327 teristics of granular material, which was first experimentally observed in (Misra and Jiang, 1997),  
328 and are generally attributed to the randomness of the granular structure. It is remarkable, therefore,  
329 to observe similar fluctuations in this rather simple grain-string with regularly spaced grains and  
330 nominally uniform interconnections whose genesis could be possibly traced to mechanical features  
331 of grain-pair interactions. It is also interesting to note that the levels of fluctuations are close for  
332 both displacement components.

333 In Figure 9(rightmost), the gray level residual map is reported for the last analyzed image. It  
334 is worth noting that the grain areas do not have clear residuals. However, the connecting beams  
335 are clearly visible, which means that their kinematics was not properly captured. These two points  
336 show that in the macroscale analysis, the overall deformations are correctly captured. However,  
337 the details of the connecting parts of the grains were not. In the absence of complete knowledge of  
338 microstructure and micromechanics (hence a possibility for microscale DIC analyses), macroscale  
339 DIC provides significant clues, albeit with an incomplete description, regarding the effect of the  
340 underlying micro-mechano-morphology. For the analyzed grain-string, tantalizing transverse dis-  
341 placement fields and longitudinal fluctuations were extracted, although specific details may only  
342 be revealed in microscale or mesoscale analyses as shown in the subsequent results.

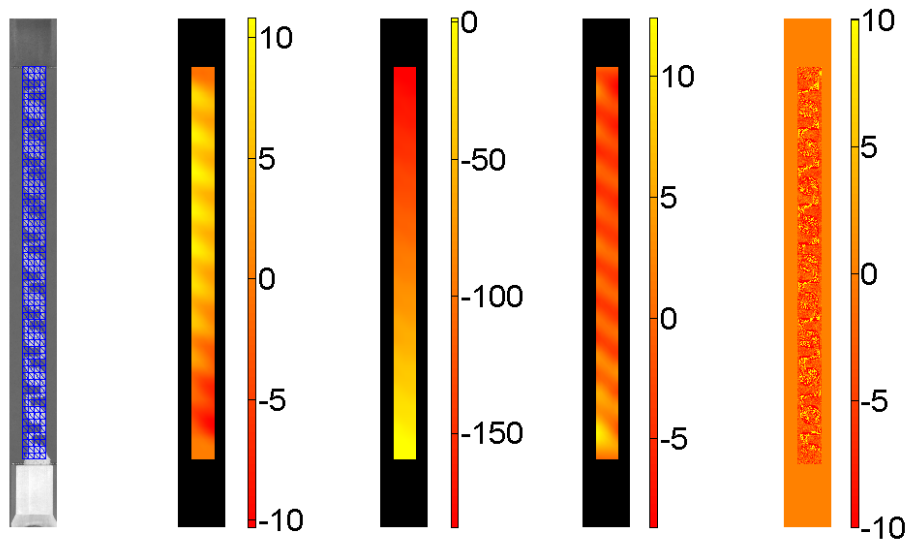


**Figure 9:** Mesh laid over the reference picture for the macroscale analysis of the speckled surface (left-most). Transverse displacement (expressed in px) field for the last analyzed picture (left). Corresponding longitudinal displacement (expressed in px) field (middle) and displacement fluctuations once the mean strain contribution was taken out (right). Gray level residual field (rightmost)

## 343 5.2. Mesoscale Analysis

344 The mesoscale analyses dealt rigid body motions of the grains, thus the kinematics was reduced  
 345 to 3 DOFs for each grain (Section 4.2). Figure 10 shows the change of the grain-displacement  
 346 components and grain-rotation about their barycenters, where different curves represent different  
 347 overall extensions of the grain-string. Since the boundary grains were held tightly in the grips  
 348 of the loading frame, the transverse displacement and the rotations of the boundary grains were  
 349 zero. It is interesting to note that the longitudinal displacement was predominantly linear with  
 350 respect to the grain number (also with grain-location since they are equally spaced). This trend  
 351 was already observed in the macroscale results (Figure 9). To confirm this observation, the mean  
 352 strain contribution was taken out to report the remaining fluctuations (Figure 10(c)). Interestingly,  
 353 such fluctuations consistently increased with the applied load (*i.e.*, their pattern was set early on

354 and is a further confirmation that it is the signature of the underlying mesostructure).

355 The transverse displacement, on the other hand, has a sinusoidal-like pattern that formed as the  
356 applied displacement increased. Similarly, grain-rotations (due to the asymmetry of the underlying  
357 structure of grain interconnections, or in an alternative interpretation the grain-pair mechanical  
358 interactions, with respect to the loading direction) increased with the applied overall extension. It  
359 is also noteworthy that the grain rotations are coherent in the counter-clockwise direction, that is,  
360 all the grain rotations are in the same orientation as opposed to gear-like opposite rotations, which  
361 are also observed in granular systems (Kuhn and Bagi, 2004; Harrington et al., 2014; Wang et al.,  
362 2021). It is further observed that the system supports grain-rotation gradients such that energy is  
363 stored in grain-pair relative rotations.

## Multiscalar DIC Analyses Reveal Non-standard Deformation Mechanisms

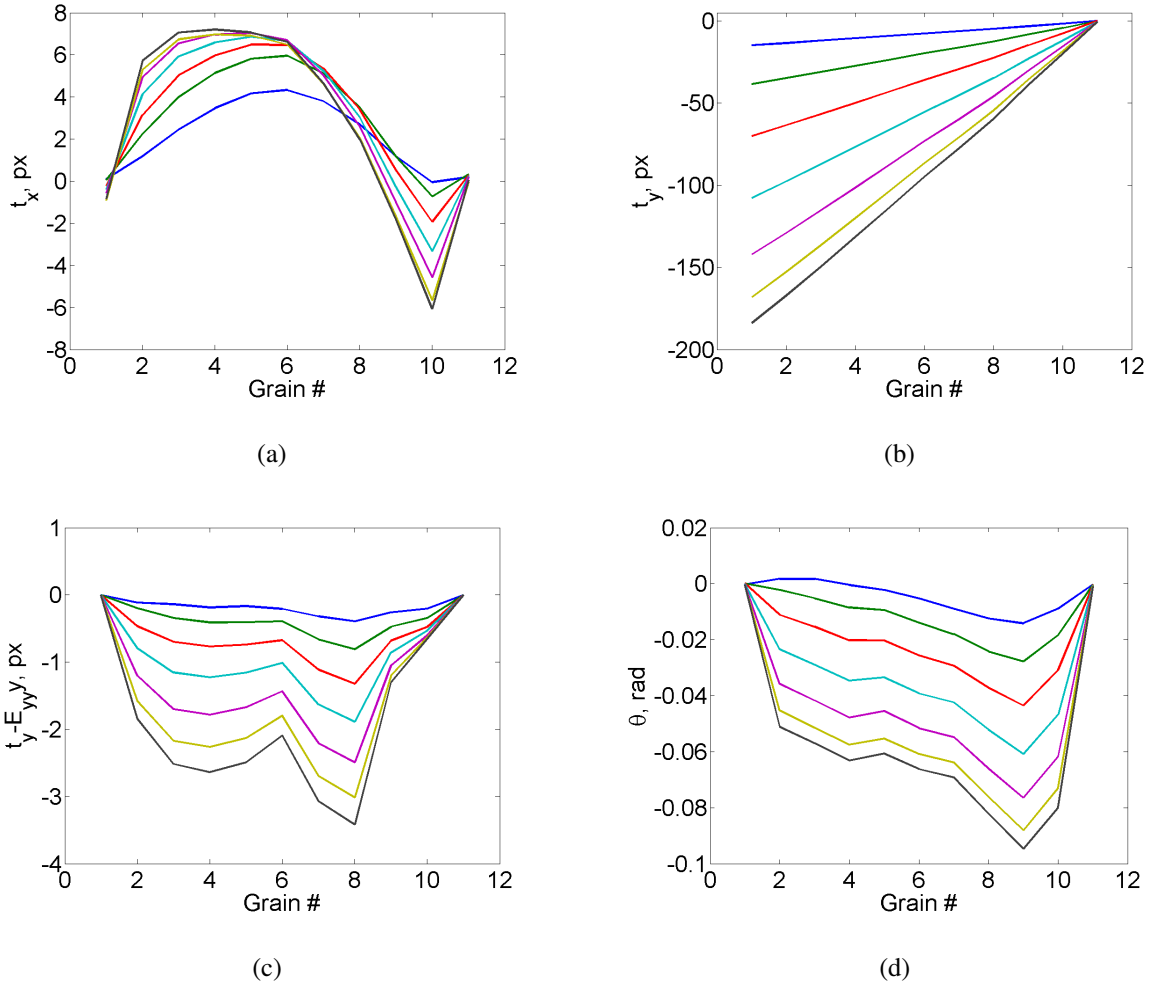


**Figure 10:** Change of the transverse translation (a), longitudinal translation (b), fluctuations of the longitudinal translation (c), and rotation (d) of the eleven grains for all analyzed images of the speckled surface (for line color, refer to Figure 7)

364 To confirm the granular nature of the deformation behavior of the granular-string, the findings  
 365 from the analysis with 6 DOFs per grain are shown in Figure 11. The rigid body translations are  
 366 virtually identical to those observed in Figure 10. The normal components of the deformation gra-  
 367 dient tensor (*i.e.*,  $F_{xx}$  and  $F_{yy}$ ) have amplitudes that are less than 1% with respect to unity (*i.e.*, very  
 368 low levels of normal strains). Conversely, the off-diagonal components are virtually identical in  
 369 absolute value indicating very small shear strains and mainly rigid body rotations. These observa-  
 370 tions also explain why the gray level residuals were very close for the analyses with 3 and 6 DOFs

371 per grain (Figure 7).

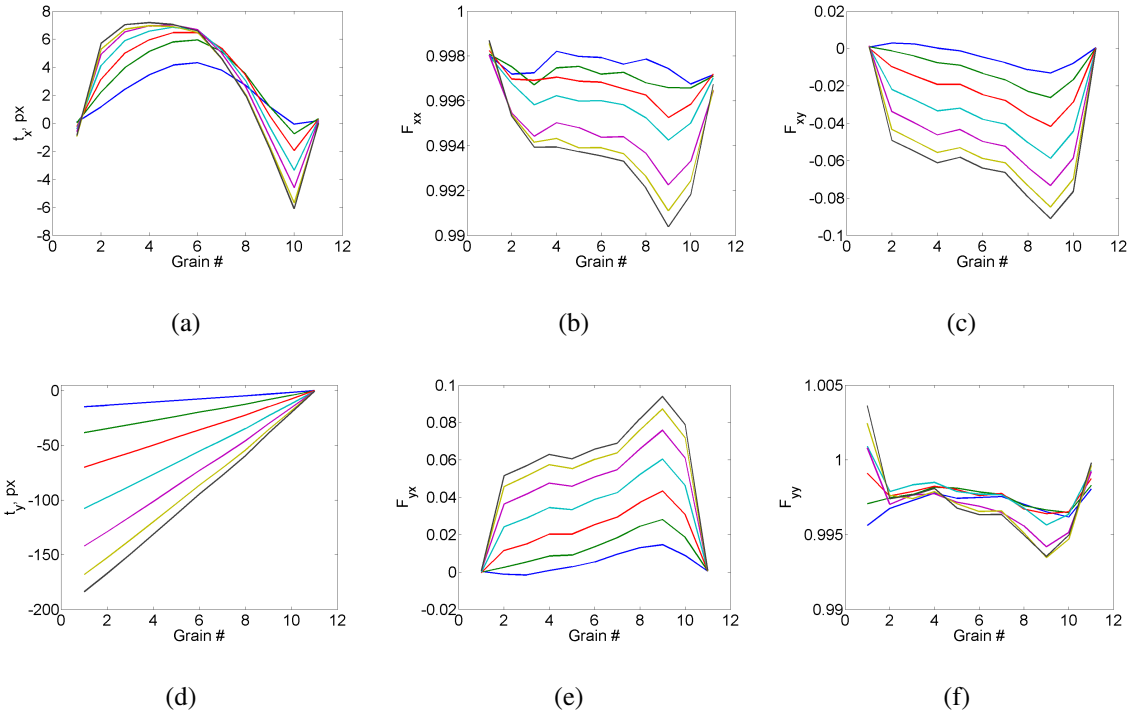


**Figure 11:** Evolution of the six degrees of freedom of the eleven grains for all analyzed images of the speckled surface. Each curve corresponds to a different-level of applied overall extension (for line color, refer to Figure 7)

### 372 5.3. Microscale Analysis

373 For the grain-string, the details of the microstructure, particularly with respect to their inter-  
 374 connections, are known. Thus, microscale DIC analyses were performed to better capture the  
 375 local details of deformations (Figure 12). In that case, the mesh was tailored to fit the initial ge-  
 376 ometry with the backtracking procedure (Figure 12(leftmost)). The transverse displacements are  
 377 now clearly revealed (Figure 12(left)) in comparison to the macroscale result (Figure 9(left)). The  
 378 transverse motions were strongly influenced by the underlying geometry of the granular string.  
 379 The longitudinal displacements (Figure 12(right)) seem to remain close to their macroscale esti-  
 380 mates (Figure 9(middle)). However, once the mean strain component was subtracted, significant  
 381 fluctuations are observed, which are primarily concentrated in the grain interconnections further



382 confirming that their likely origin is due to the features of grain-pair mechanical interactions. Need-  
 383 less to say, the results at the microscale are more detailed as well as reliable as indicated by the  
 384 gray level residual map that no longer shows high levels for the connecting parts and remains low  
 385 in the grains as well.

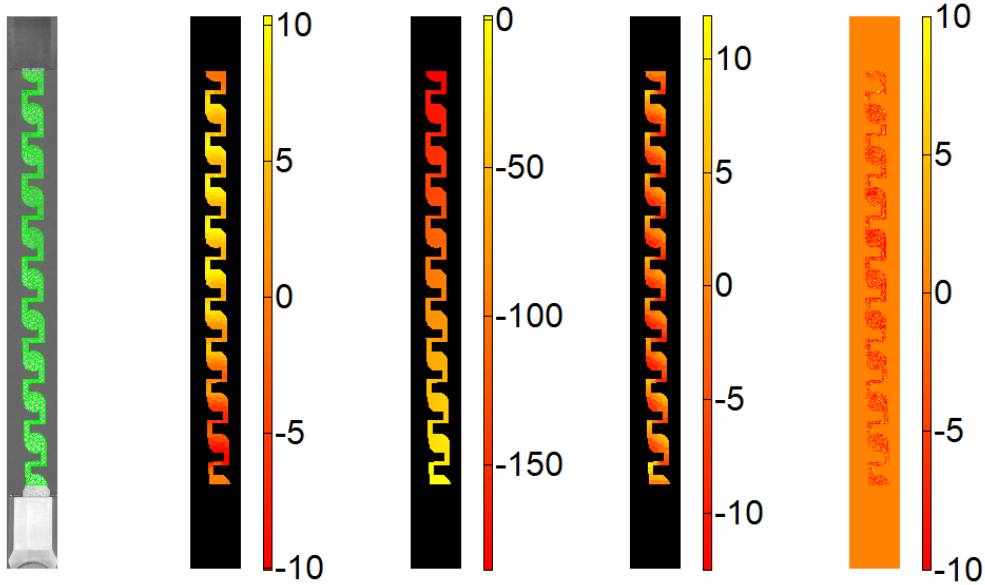


**Figure 12:** Mesh laid over the reference picture for the microscale analysis of the speckled surface (left-most). Transverse displacement (expressed in px) field for the last analyzed picture (left). Corresponding longitudinal displacement (expressed in px) field (middle) and displacement fluctuations (right) once the mean strain contribution was taken out. Gray level residual field (rightmost)

386 From this first set of results at the microscale arise two additional questions. First, given the  
 387 fineness of the interconnections, regularized DIC was required. There is still a choice to be made  
 388 when the regularization length  $\ell_{reg}$  is greater than the element (as was the case herein). Different  
 389 analyses were run starting with the largest length (*i.e.*, 800 px). The next DIC run was carried out  
 390 by dividing the regularization length by 2 and initializing the calculations with the results obtained  
 391 with the previous regularization length. This relaxation procedure (Tomičević et al., 2013) was  
 392 carried out down to a regularization length of 50 px. Figure 13 shows the change of the equilibrium  
 393 residual  $\varrho_m$  as a function of the registration residual  $\varrho_c$  for the 7 analyzed pictures. As more weight

394 was put on the penalty term (*i.e.*,  $\ell_{reg}$  was increased), the equilibrium residuals were lowered,  
 395 and the RMS gray level residuals started to increase. This is a typical feature of such regularized  
 396 schemes (Hansen, 2010).

397 Further, it is interesting to note that for the first two pictures, the gray levels residuals remained  
 398 essentially constant for any selected regularization length. This observation shows that the under-  
 399 lying hypothesis of Hencky elasticity was valid. Conversely, from the third picture on, this trend is  
 400 non longer observed, and the gray level residuals increased more significantly as the regularization  
 401 length was increased, which indicates a model error. This effect means that nonlinear phenomena  
 402 occurred and were not accounted for by Hencky elasticity. As a consequence, the chosen regular-  
 403 ization length should not be too high. In the present case, a length of 100 vx was selected, which  
 404 was a good compromise between the two cost functions, particularly for revealing the deformation  
 405 trends.

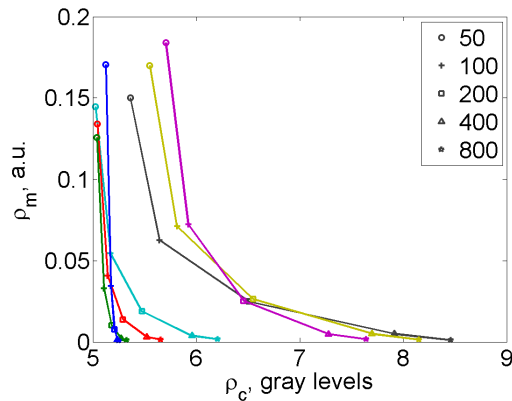


**Figure 13:** Equilibrium residual  $\rho_m$  vs. RMS gray level residuals  $\rho_c$  for different regularization lengths  $\ell_{reg}$  (expressed in vx) and all analyzed pictures (for line color, refer to Figure 8)

406 The second question is related to the deformation mechanisms of the interconnections that  
 407 led to non classical results at the meso- and macroscales. For this type of investigation, the 16 px  
 408 discretization was too coarse as there were at most 2 elements in the thickness of the interconnecting  
 409 beams (Figure 4(right)). A very fine mesh was then constructed with a mean element size of  
 410 3 px, which allowed for a least six elements in the thickness of each beam. In terms of overall

411 displacement fields, there were not many differences given their very high amplitudes. However,  
412 using this very fine mesh more local strain details could be better captured. In the following results,  
413 the Green-Lagrange strains are reported. They were assessed from the deformation gradient tensor,  
414 which was obtained from the exact derivation of the T3 shape functions (*i.e.*, they are uniform over  
415 each element).

416 The transverse Green-Lagrange strain field is shown in Figure 13(leftmost) for the last analyzed  
417 picture. Very low strain levels are observed in the vertical beams and the grains. The horizontal  
418 beams of each interconnections undergo transverse strain that are consistent with flexure. This  
419 result was expected from the mesoscale analyses which show the transverse motion and rotation  
420 of grains. Figure 13(left) shows the corresponding longitudinal strain field. These strain fields are  
421 consistent with the flexure of the vertical beams, whereas the horizontal beams mostly elongated.  
422 In terms of shear strains (Figure 13(right)), they were more important in the horizontal beams than  
423 in the vertical ones. In the grains, all strain components were very low in magnitude, which further  
424 validates the hypothesis of rigid body motions.

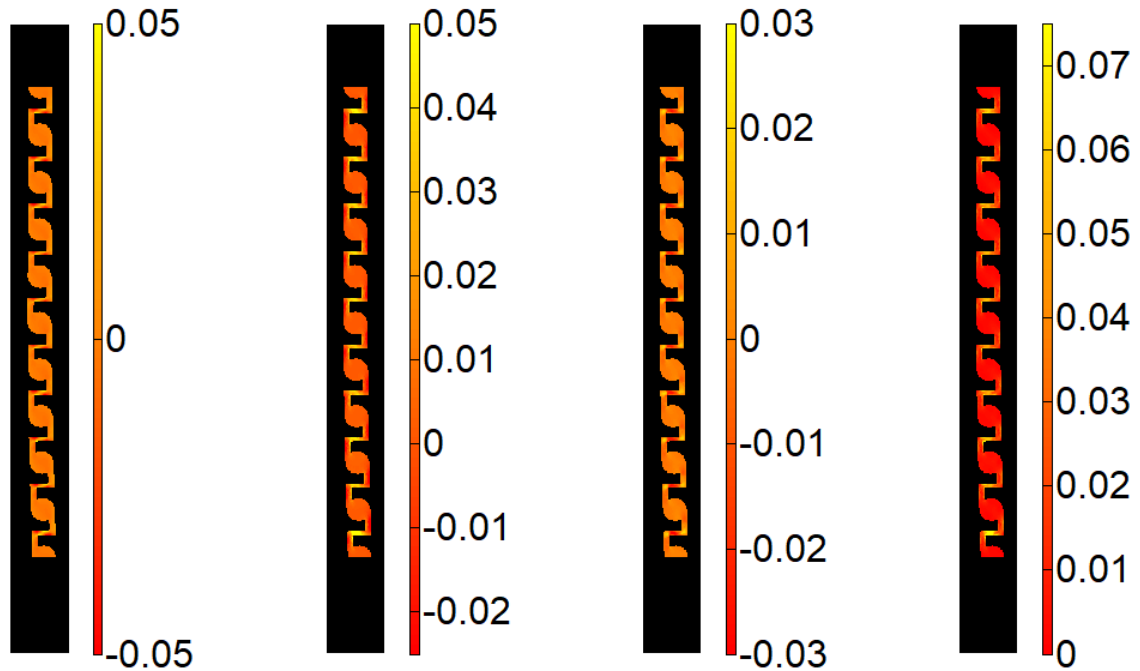


**Figure 14:** Transverse strain field for the last analyzed picture (leftmost). Corresponding longitudinal (left) and shear (right) strain fields for the last analyzed picture. Equivalent elastic strain field (rightmost)

425 Last, to assess the distribution of strain energy, the equivalent elastic strain field is shown in  
 426 Figure 13(rightmost). The latter corresponds to the square root of twice the strain energy (computed  
 427 with a plane stress assumption) divided by the Young's modulus. Most of the elastic energy was  
 428 stored in the horizontal beams, whose deformation was a combination of extension and flexure.  
 429 This result shows that the grain-string can be treated as a granular matter composed of nearly  
 430 rigid elements (or grains) and the elastic strain energy is stored in the deformable mechanisms  
 431 represented through interconnections or interfaces between grains. Furthermore, the deformation  
 432 of the grain string is controlled by that of the interconnections, and therefore can be modulated by  
 433 varying the geometrical attributes of the interconnections.

## 434 6. Conclusion

435 The deformation behavior of a chiral granular string was analyzed using DIC devised for three  
 436 spatial scales, termed here as macro, meso and micro. The registration residuals of the kinematic

437 bases probed at the different scales showed very low levels at two of the chosen scales (namely,  
438 micro- and meso-scales) indicating that the deformation mechanisms were properly captured. Al-  
439 though the macroscale description was not as trustworthy, it, nevertheless, provided the necessary  
440 initial estimates that were very useful for analyses at lower scales. This choice was particularly  
441 important since the displacement increments between adjacent images were very high.

442 It is also noteworthy that multiscalar analyses have the advantage of elucidating deformation  
443 mechanisms that may not be clearly discernible at the macroscale or whose implication at the  
444 macroscale is not clear if the focus is only on the microscale. Remarkably, a physical material  
445 with microstructure is more intricate than its mathematical model. It may encompass deformation  
446 mechanisms that are usually overlooked when modeling. Multiscale DIC analyses offer points of  
447 comparison to the model predictions, with which a validation or a need for a refined kinematic  
448 description can be concluded.

449 For the grain-string analyzed in this work, the performed DIC analyses revealed certain non-  
450 standard deformation mechanisms whose genesis is likely to be the chiral-nature of the mechanical  
451 response of grain-pair interconnections. As the granular string was subjected to extension, coherent  
452 grain rotations (as opposed to gear-like) and transverse grain displacements were observed which  
453 increased in magnitude as the loading progresses. In addition, fluctuations from the linear field  
454 in the longitudinal displacements were observed. The quantification of the deformation mecha-  
455 nisms in the interconnections with results utilizing a very fine mesh at the microscale confirm the  
456 kinematic bases for mesoscale analysis. Further, these microscale results indicate that the nature  
457 and magnitude of the non-standard deformations is controlled by the mechanics of grain-pair in-  
458 teractions, which in turn is governed by the geometrical parameters of the grain interconnections  
459 for a given fabricated (meta)material. These aspects will be further explored experimentally and  
460 theoretically in forthcoming works.

461 **Acknowledgements**

462 This research is supported in part by the United States National Science Foundation grant  
463 CMMI-1727433.

464 **Credit authorship statement**

465 NN performed the experiments, MDA assisted in granular string design, AM conceived the  
466 idea, FH devised the DIC methodology and performed the DIC analyses. All authors contributed to  
467 the discussion of all aspects of this work. NN, MDA, AM and FH wrote and edited the manuscript.

468 **Compliance with Ethical Standards**

469 The authors have no conflict of interest to declare.

470 **References**

- 471 Alderson, A., Alderson, K., Attard, D., Evans, K., Gatt, R., Grima, J., Miller, W., Ravirala, N., Smith, C., Zied, K., 2010. Elastic constants of 3-, 4-  
472 and 6-connected chiral and anti-chiral honeycombs subject to uniaxial in-plane loading. *Composites Science and Technology* 70, 1042–1048.
- 473 Alibert, J.J., Seppecher, P., dell’Isola, F., 2003. Truss Modular Beams with Deformation Energy Depending on Higher Displacement Gradients.  
474 *Mathematics and Mechanics of Solids* 8, 51–73.
- 475 ASD-STAN prEN 4861 P1, 2018. Metrological assessment procedure for kinematic fields measured by digital image correlation. /www.asd-  
476 stan.org/downloads/asd-stan-pren-4861-p1.
- 477 Auger, P., Lavigne, T., Smaniotto, B., Spagnuolo, M., dell’Isola, F., Hild, F., 2021. Poynting Effects in Pantographic Metamaterial Captured via  
478 Multiscale DVC. *Journal of Strain Analysis for Engineering Design* (in press) DOI: 10.1177/0309324720976625.
- 479 Barchiesi, E., dell’Isola, F., Bersani, A., Turco, E., 2021. Equilibria determination of elastic articulated duoskelion beams in 2d via a riks-type  
480 algorithm. *International Journal of Non-Linear Mechanics* 128, 103628.
- 481 Barchiesi, E., Spagnuolo, M., Placidi, L., 2019. Mechanical metamaterials: a state of the art. *Mathematics and Mechanics of Solids* 24, 212–234.
- 482 Biswas, R., Poh, L., Shedbale, A., 2020. A micromorphic computational homogenization framework for auxetic tetra-chiral structures. *Journal of*  
483 *the Mechanics and Physics of Solids* 135, 103801.
- 484 Bruno, L., Decuzzi, P., Gentile, F., 2016. Stress distribution retrieval in granular materials: A multi-scale model and digital image correlation  
485 measurements. *Optics and Lasers in Engineering* 76, 17–26.
- 486 Chen, Y., Frenzel, T., Guenneau, S., Kadic, M., Wegener, M., 2020. Mapping acoustical activity in 3d chiral mechanical metamaterials onto  
487 micropolar continuum elasticity. *Journal of the Mechanics and Physics of Solids* 137, 103877.
- 488 Chen, Y., Liu, X., Hu, G., Sun, Q., Zheng, Q., 2014. Micropolar continuum modelling of bi-dimensional tetrachiral lattice. *Proceedings of the*  
489 *Royal Society A* 470, 20130734.
- 490 Claire, D., Hild, F., Roux, S., 2004. A finite element formulation to identify damage fields: The equilibrium gap method. *Int. J. Num. Meth. Engng.*  
491 61, 189–208.

## Multiscalar DIC Analyses Reveal Non-standard Deformation Mechanisms

- 492 Cundall, P.A., Strack, O., 1979. A discrete numerical model for granular assemblies. *Géotechnique* 29, 47–65.
- 493 De Angelo, M., Placidi, L., NejadSadeghi, N., Misra, A., 2020. Non-standard Timoshenko beam model for chiral metamaterial: Identification of  
494 stiffness parameters. *Mechanics Research Communications* 103, 103462.
- 495 dell’Isola, F., Seppecher, P., Spagnuolo, M., Barchiesi, E., Hild, F., Lekszycki, T., Giorgio, I., Placidi, L., Andreaus, U., Cuomo, M., Eugster, S.,  
496 Pfaff, A., Hoschke, K., Langkemper, R., Turco, E., Sarikaya, R., Misra, A., De Angelo, M., D’Annibale, F., Bouterf, A., Pinelli, X., Misra, A.,  
497 Desmorat, B., Pawlikowski, M., Dupuy, C., Scerrato, D., Peyre, P., Laudato, M., Manzari, L., Göransson, P., Hesch, C., Hesch, S., Franciosi, P.,  
498 Dirrenberger, J., Maurin, F., Vangelatos, Z., Grigoropoulos, C., Melissinaki, V., Farsari, M., Muller, W., Abali, E., Liebold, C., Ganzosch, G.,  
499 Harrison, P., Drobnicki, R., Igumnov, L., Alzahrani, F., Hayat, T., 2019. Advances in Pantographic Structures: Design, Manufacturing, Models,  
500 Experiments and Image Analyses. *Continuum Mechanics and Thermodynamics* 31, 1231–1282.
- 501 dell’Isola, F., Barchiesi, E., Misra, A., 2020. Naïve Model Theory: its applications to the Theory of Metamaterials Design, in: dell’Isola, F.,  
502 Steigmann, D. (Eds.), *Discrete and Continuum Models for Complex (Meta) Materials*, Cambridge University Press. pp. 141–196.
- 503 Dirrenberger, J., Forest, S., Jeulin, D., Colin, C., 2011. Homogenization of periodic auxetic materials. *Procedia Engineering* 10, 1847–1852.
- 504 Drescher, A., de Josselin de Jong, G., 1972. Photoelastic verification of a mechanical model for the flow of a granular material. *Journal of the*  
505 *Mechanics and Physics of Solids* 20, 337–340.
- 506 Duan, S., Wen, W., Fang, D., 2018. A predictive micropolar continuum model for a novel three-dimensional chiral lattice with size effect and  
507 tension-twist coupling behavior. *Journal of the Mechanics and Physics of Solids* 121, 23–46.
- 508 Frenzel, T., Kadic, M., Wegener, M., 2017. Three-dimensional mechanical metamaterials with a twist. *Science* 358, 1072–1074.
- 509 Geuzaine, C., Remacle, J.F., 2009. Gmsh: a three-dimensional finite element mesh generator with built-in pre- and post-processing facilities.  
510 *International Journal for Numerical Methods in Engineering* 79, 1309–1331.
- 511 Giorgio, I., dell’Isola, F., Misra, A., 2020. Chirality in 2D Cosserat media related to stretch-micro-rotation coupling with links to granular microme-  
512 chanics. *International Journal of Solids and Structures* 202, 28–38.
- 513 Hall, S., Muir Wood, D., Ibraim, E., Viggiani, G., 2010. Localised deformation patterning in 2D granular materials revealed by digital image  
514 correlation. *Granular Matter* 12, 1–14.
- 515 Hansen, P., 2010. *Discrete Inverse Problems: Insight and Algorithms*. Fundamentals of algorithms series, Society for Industrial and Applied  
516 Mathematics (SIAM), Philadelphia, PA (USA). doi:10.1137/1.9780898718836.
- 517 Harrington, M., Lin, M., Nordstrom, K.N., Losert, W., 2014. Experimental measurements of orientation and rotation of dense 3D packings of  
518 spheres. *Granular Matter* 16, 185–191.
- 519 Hild, F., Misra, A., dell’Isola, F., 2021. Multiscale DIC applied to Pantographic Structures. *Experimental Mechanics* 61, 431–443.
- 520 Hild, F., Roux, S., 2012. Digital image correlation, in: Rastogi, P., Hack, E. (Eds.), *Optical Methods for Solid Mechanics. A Full-Field Approach*,  
521 Wiley-VCH, Weinheim (Germany). pp. 183–228.
- 522 Holtzman, R., Silin, D., Patzek, T.W., 2010. Frictional granular mechanics: A variational approach. *International Journal for Numerical Methods*  
523 *in Engineering* 81, 1259–1280.
- 524 iDICs, Jones, E., Iadicola, M. (Eds.), 2018. *A Good Practices Guide for Digital Image Correlation*. International Digital Image Correlation Society  
525 (iDICs), DOI: 10.32720/idics/gpg.ed1.
- 526 Jean, M., Moreau, J.J., 1987. Dynamics in the presence of unilateral contacts and dry friction: A numerical approach, in: Del Piero, G., Maceri, F.  
527 (Eds.), *Unilateral Problems in Structural Analysis — 2*, Springer Vienna, Vienna. pp. 151–196.
- 528 Kuhn, M., Bagi, K., 2004. Contact rolling and deformation in granular media. *International Journal of Solids and Structures* 41, 5793–5820.
- 529 Larsson, S., Rodríguez Prieto, J., Gustafsson, G., Håggblad, H., Jonsén, P., 2020. The particle finite element method for transient granular material

## Multiscalar DIC Analyses Reveal Non-standard Deformation Mechanisms

- 530 flow: modelling and validation. *Computational Particle Mechanics* .
- 531 Leclerc, H., Neggers, J., Mathieu, F., Hild, F., Roux, S., 2015. Correli 3.0. IDDN.FR.001.520008.000.S.P.2015.000.31500. Agence pour la  
532 Protection des Programmes, Paris (France).
- 533 Liu, X., Hu, G., Sun, C., Huang, G., 2011. Wave propagation characterization and design of two-dimensional elastic chiral metamaterial. *Journal*  
534 *of Sound and Vibration* 330, 2536–2553.
- 535 Liu, X., Huang, G., Hu, G., 2012. Chiral effect in plane isotropic micropolar elasticity and its application to chiral lattices. *Journal of the Mechanics*  
536 *and Physics of Solids* 60, 1907–1921.
- 537 Misra, A., Jiang, H., 1997. Measured kinematic fields in the biaxial shear of granular materials. *Computers and Geotechnics* 20, 267–285. *Theoretical*  
538 *and Experimental Methods for Particulate Materials*.
- 539 Misra, A., Lekszycki, T., Giorgio, I., Ganzosch, G., Müller, W., dell’Isola, F., 2018. Pantographic metamaterials show atypical poyniting effect  
540 reversal. *Mechanics Research Communications* 89, 6–10.
- 541 Misra, A., NejadiSadeghi, N., De Angelo, M., Placidi, L., 2020. Chiral metamaterial predicted by granular micromechanics: verified with 1D  
542 example synthesized using additive manufacturing. *Continuum Mechanics and Thermodynamics* 32, 1497–1513.
- 543 NejadiSadeghi, N., Misra, A., 2020. Extended granular micromechanics approach: a micromorphic theory of degree n. *Mathematics and Mechanics*  
544 *of Solids* 25, 407–429.
- 545 Poncelet, M., Somera, A., Morel, C., Jailin, C., Auffray, N., 2018. An experimental evidence of the failure of Cauchy elasticity for the overall  
546 modeling of a non-centro-symmetric lattice under static loading. *International Journal of Solids and Structures* 147, 223–237.
- 547 Poorsolhjoui, P., Misra, A., 2019. Granular micromechanics based continuum model for grain rotations and grain rotation waves. *Journal of the*  
548 *Mechanics and Physics of Solids* 129, 244–260.
- 549 Reasa, D., Lakes, R., 2019. Cosserat effects in achiral and chiral cubic lattices. *Journal of Applied Mechanics* 86, 111009.
- 550 Rechenmacher, A., 2006. Grain-scale processes governing shear band initiation and evolution in sands. *Journal of the Mechanics and Physics of*  
551 *Solids* 54, 22–45.
- 552 Réthoré, J., Roux, S., Hild, F., 2009. An extended and integrated digital image correlation technique applied to the analysis fractured samples.  
553 *European Journal of Computational Mechanics* 18, 285–306.
- 554 Richefeu, V., Combe, G., 2020. The particle image tracking technique: An accurate optical method for measuring individual kinematics of rigid  
555 particles. *Strain* 56, e12362.
- 556 Richefeu, V., Combe, G., Viggiani, G., 2012. An experimental assessment of displacement fluctuations in a 2d granular material subjected to shear.  
557 *Géotechnique Letters* 2, 113–118.
- 558 Schneebeli, G., 1956. Une analogie mécanique pour les terres sans cohésion. *Comptes Rendus de l’Academie des Sciences* 243, 125–126.
- 559 Spadoni, A., Ruzzene, M., Gonella, S., Scarpa, F., 2009. Phononic properties of hexagonal chiral lattices. *Wave Motion* 46, 435–450.
- 560 Surjadi, J., Gao, L., Du, H., Li, X., Xiong, X., Fang, N., Lu, Y., 2019. Mechanical metamaterials and their engineering applications. *Advanced*  
561 *Engineering Materials* 21, 1800864.
- 562 Sutton, M., 2013. Computer vision-based, noncontacting deformation measurements in mechanics: A generational transformation. *Applied Me-*  
563 *chanics Reviews* 65, 050802.
- 564 Tikhonov, A., Arsenin, V., 1977. *Solutions of ill-posed problems*. J. Wiley, New York (USA).
- 565 Tomičević, Z., Hild, F., Roux, S., 2013. Mechanics-aided digital image correlation. *Journal of Strain Analysis for Engineering Design* 48, 330–343.
- 566 Turco, E., dell’Isola, F., Misra, A., 2019. A nonlinear Lagrangian particle model for grains assemblies including grain relative rotations. *International*  
567 *Journal for Numerical and Analytical Methods in Geomechanics* 43, 1051–1079.



- 568 Vardoulakis, I., 2019. *Cosserat Continuum Mechanics – With Applications to Granular Media*. volume 87 of *Lecture notes in applied and compu-*  
569 *tational mechanics*. Springer, Cham (Switzerland).
- 570 Wang, D., NejadSadeghi, N., Li, Y., Shekhar, S., Misra, A., Dijkstra, J., 2021. Rotational diffusion and rotational correlations in frictional  
571 amorphous disk packings under shear. *Soft Matter* 17, 7844–7852.
- 572 Wu, W., Hu, W., Qian, G., Liao, H., Xu, X., Berto, F., 2019. Mechanical design and multifunctional applications of chiral mechanical metamaterials:  
573 A review. *Materials Design* 180, 107950.

## 574 7. Appendix B

575 In the following, the results obtained for the extensional test are reported when the dotted sur-  
576 face was monitored (Figure 15).



Figure 15: Cropped gray level images of the extensional test with dotted grains

### 577 7.1. Multiscalar DIC Analyses

578 Figure 16 show the three meshes for the convergence analysis at the macroscale. The element  
579 sizes were 91, 37, and 23 px.

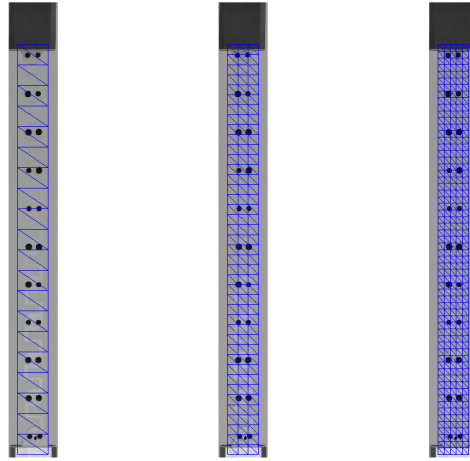


Figure 16: Three meshes used for the DIC analyses at the macroscale of the dotted (b) surface

580 Figure 17 shows that the RMS residuals are higher (*i.e.*, between 1.5 and 5 times) than the level  
 581 associated with acquisition noise (*i.e.*, 1.2 gray level). They also grew as the applied displacement  
 582 amplitude increased. The same remarks applied for the macroscale analyses of the speckled surface  
 583 (Figure 6). This observation shows that, for both tests, the macroscopic kinematic bases were not  
 584 able to properly capture the complexity of local displacement fields induced by the geometry of the  
 585 metamaterial as the applied displacement increases.

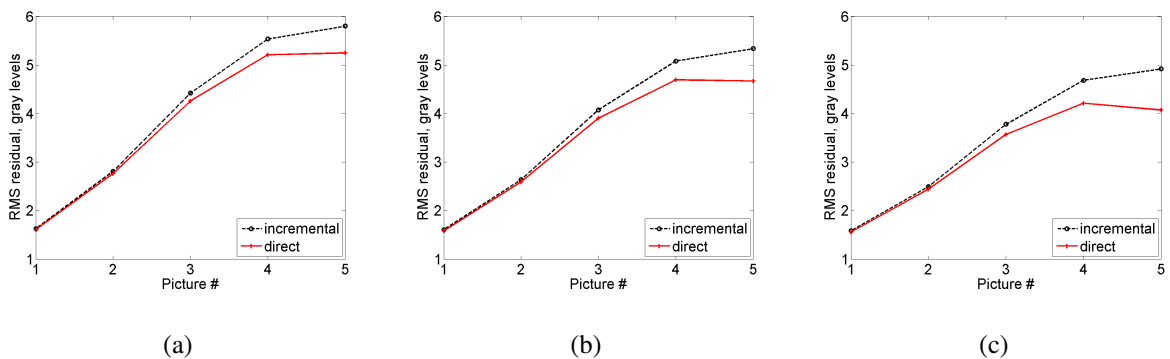


Figure 17: RMS gray level residuals for the three meshes of the dotted surface (Figure 16) and the two DIC routes

586 When following the backtracking procedure for the dotted surface (Figure 18(leftmost)), the  
 587 dots were also considered in the mask that was used for registration purposes (Figure 18(left)).  
 588 The inclusion of dots within the mask is expected to provide more accurate registration. This could  
 589 further improve the accuracy of the measured deformation fields especially in the lateral direction  
 590 (transverse to the extension direction). It is noted that the accuracy of lateral deformations are  
 591 of particular interest in this analysis (Misra et al., 2020). Figure 18(right)) shows the backtracked  
 592 mesh. The same operation was carried out for the 4-element zones of discrete approaches following  
 593 the motion of each dot (Figure 18(rightmost)).



**Figure 18:** Backtracked meshes for microscale DIC of the dotted surface. The image of the reference configuration (leftmost) is registered with that of the nominal configuration (left) using the auxiliary mesh shown in blue. The backtracked mesh is laid over the reference image (right). The grain centers (red crosses) are also depicted. Similarly, the 4-element zones about each dot are also backtracked (rightmost)

594 The mean element size was equal to 16 px for this last mesh. For the dotted surface, the RMS  
 595 residuals were even lower (*i.e.*, less than 2 times the level due to acquisition noise) than for the  
 596 speckled surface (*i.e.*, of the order of 2.3 the level due to acquisition noise). However, it should  
 597 not be concluded that in that case the results are more trustworthy since the surface patterns were

598 completely different. However, it can be concluded that in both cases, the kinematics is very well  
 599 captured by such analyses. If deformation details were to be sought, the mesh should be further  
 600 refined.

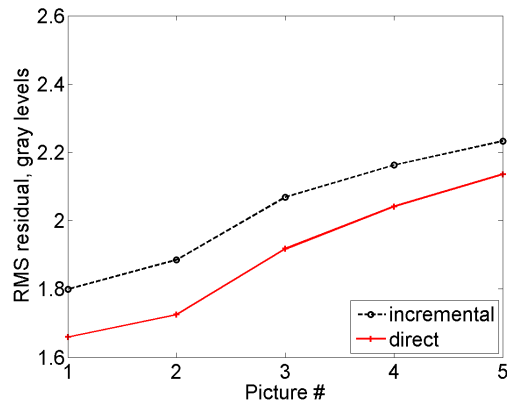


**Figure 19:** RMS gray level residuals for the DIC analyses at the microscale of the dotted surface

601 For the grain-scale analyses with 3 DOFs, a ratio 1.5 to less than 3 is observed for the RMS  
 602 residuals when related to acquisition noise (Figure 20). These results prove that the selected kine-  
 603 matics is able to better capture the underlying motions of the grains. For the dotted surface, the 6  
 604 DOF analyses was not sought. Instead, each dot was individually tracked by considering 4-element  
 605 zones arranged about each dot center. These analyses are far more delicate and sensitive when the  
 606 element length is decreased because not much contrast is available apart from the dot edges. This  
 607 remark explains why the incremental calculations were not able to converge to similar solutions as  
 608 direct analyses. For the direct analyses, the RMS residuals did not vary much and were low enough  
 609 (*i.e.*, about 2.5 times the level associated with acquisition noise) to deem the measurements reliable.

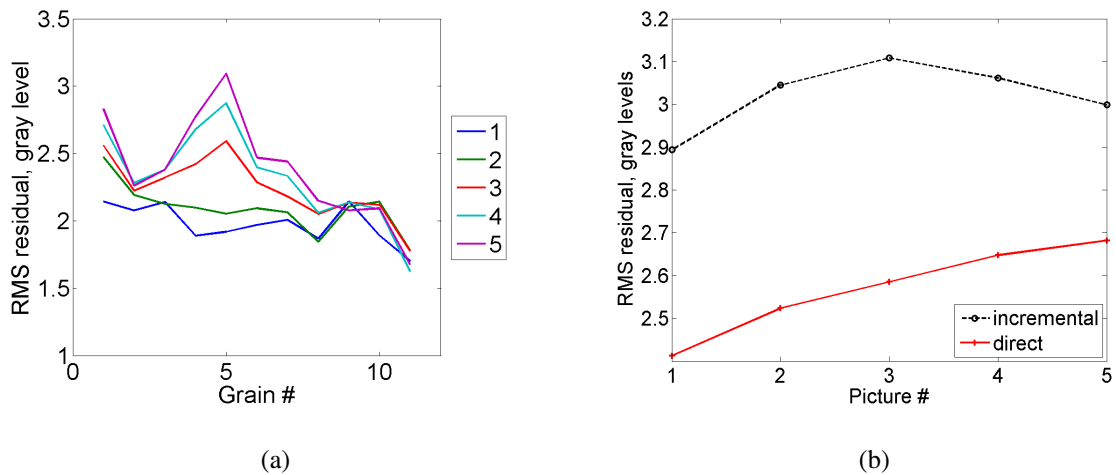


**Figure 20:** RMS gray level residuals for grain-scale (a) and local (b) DIC analyses of the dotted surface

## 7.2. Results for the Dotted Surface

The DIC results obtained with the different DIC approaches for the dotted surface are described. It is noted that these calculations are far more delicate as the surface contrast is no longer evenly distributed as in the previous case. However, the implemented DIC approach (using appropriate regularization) was able to extract many details of the deformation behavior as described in the following sections.

### 7.2.1. Macroscale Analysis

As mentioned above, the analyses at the macroscale were possible due to the regularization strategy used herein since most of the contrast is provided by the  $2 \times 11$  black dots (Figure 21(left-most)). Interestingly, even for the quality of the prepared dotted surface, the results are similar to those for the speckled surface. Consequently, the observation at the macroscale are the same as before. It is worth noting, though, that the contours of transverse displacements (Figure 21(left)) and longitudinal displacements once the mean strain contribution was taken out (Figure 21(right)) are inclined in the opposite direction. Similarly, the sign of the transverse displacements is also inverted. These two effects are due to the fact that the back face was observed instead of the front face. Clearly, the granular string is not invariant to mirror transformations about the vertical axis

626 and this aspect is reflected in the sign of measured displacements.

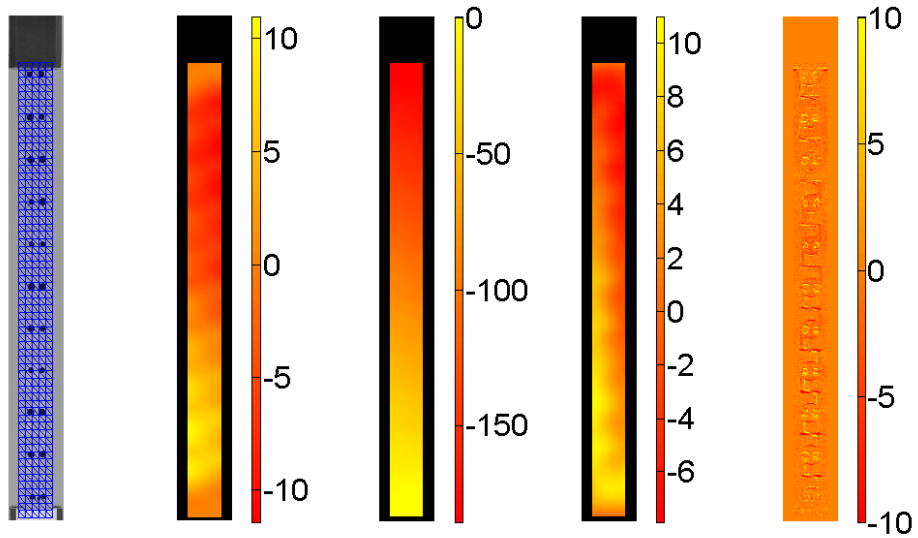


**Figure 21:** Mesh laid over the reference picture for the macroscale analysis of the dotted surface (left-most). Transverse displacement (expressed in px) field for the last analyzed picture (left). Corresponding longitudinal displacement (expressed in px) field (middle) and displacement fluctuations once the mean strain contribution was taken out (right). Gray level residual field (rightmost)

### 627 7.2.2. *Microscale Analysis*

628 The general features observed for the transverse displacement field and from the longitudinal  
 629 displacement fluctuations are confirmed by microscale analyses with 16 px elements (Figure 22).  
 630 For the longitudinal displacement field, the same type of complexity is noted as for the speckle  
 631 pattern. All these interpretations could be made since the gray level residuals remained very low  
 632 even for such high displacement amplitudes.

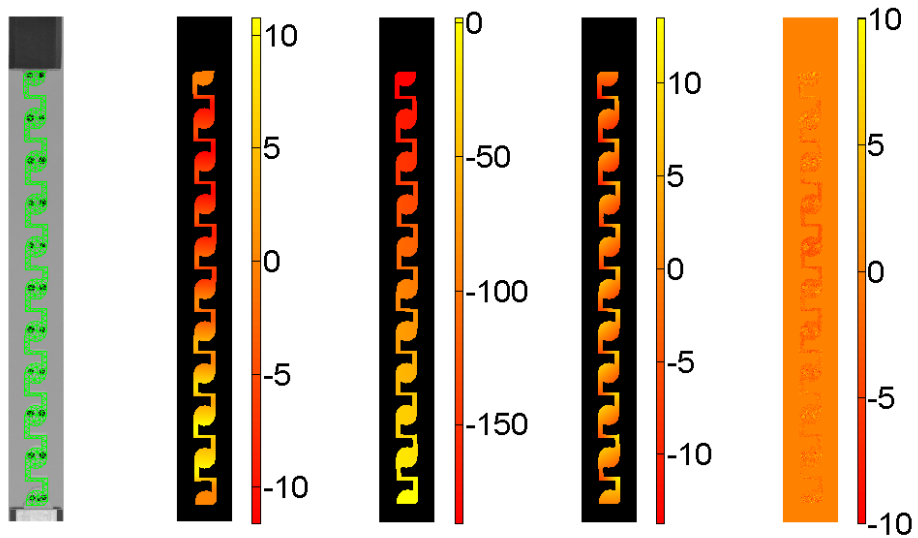


**Figure 22:** Mesh laid over the reference picture for the microscale analysis of the dotted surface (left-most). Transverse displacement (expressed in px) field for the last analyzed picture (left). Corresponding longitudinal displacement (expressed in px) field (middle) and displacement fluctuations once the mean strain contribution was taken out (right). Gray level residual field (rightmost)

633 In addition, the strain fields shown in Figure 23 exhibit the same trends as observed for the  
 634 speckle pattern (Figure 14) for a refined mesh with 3 px elements. In particular, identical deforma-  
 635 tion mechanisms and strain levels occurred in this new analysis.

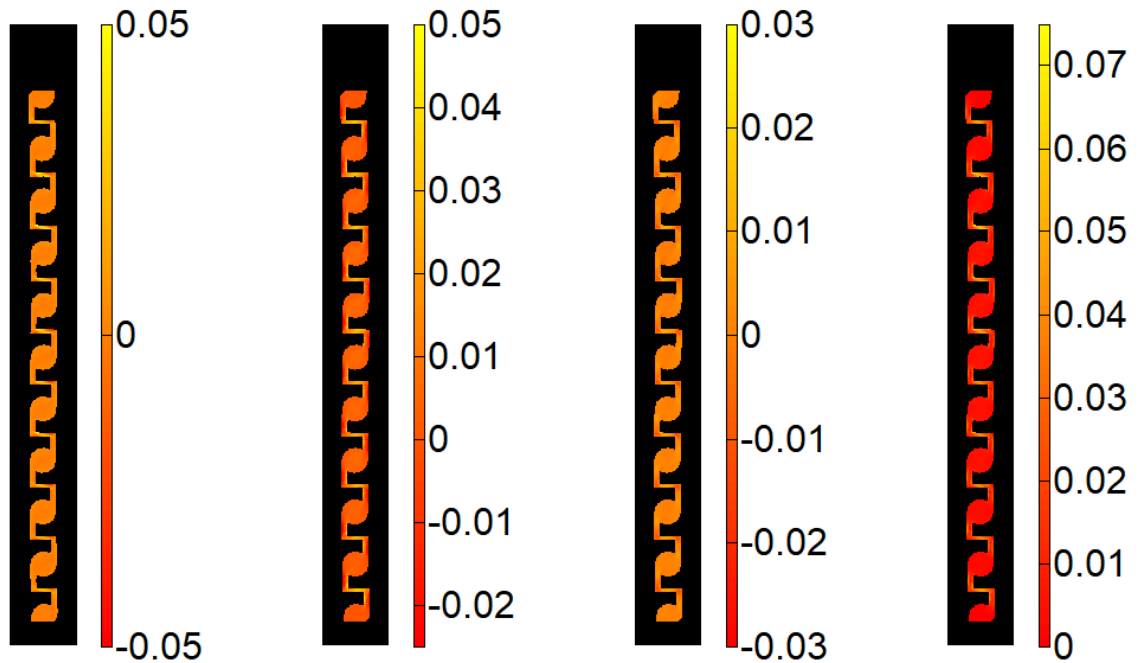


Figure 23: Transverse strain field for the last analyzed picture of the dotted surface (leftmost). Corresponding longitudinal (left), shear (right), and equivalent elastic strain field (rightmost)

### 636 7.2.3. Mesoscale Analysis

637 In Figure 24, the changes of the 3 DOFs per grain and for the 5 images are reported. It is  
 638 worth noting that the maximum amplitude was as high as in the previous test for which 7 pic-  
 639 tures were available. The present case is therefore even more challenging. However, thanks to the  
 640 initialization strategy, convergence was fast and the residuals were sufficiently low to deem these  
 641 results trustworthy. The transverse displacements are anti-symmetric with respect to the middle  
 642 grain, which was not the case for the speckled surface (Figure 10). Similarly, the longitudinal  
 643 displacement fluctuations are anti-symmetric as well in contrast to what was observed previously.  
 644 Such differences can be explained by the fact that the dotted pattern corresponds to the first cycle,  
 645 and the speckle pattern to the second cycle (opposite sides were monitored with a single camera).  
 646 Some minor plasticity and damage may have occurred during these two cycles. The sample was  
 647 unmounted between the two cycles (one week apart) so the application of boundary conditions may  
 648 have changed a bit. Last, the misalignment of the camera in terms of verticality and the differences



649 in the choice of coordinate system for the two DIC analyses may also have a small influence.

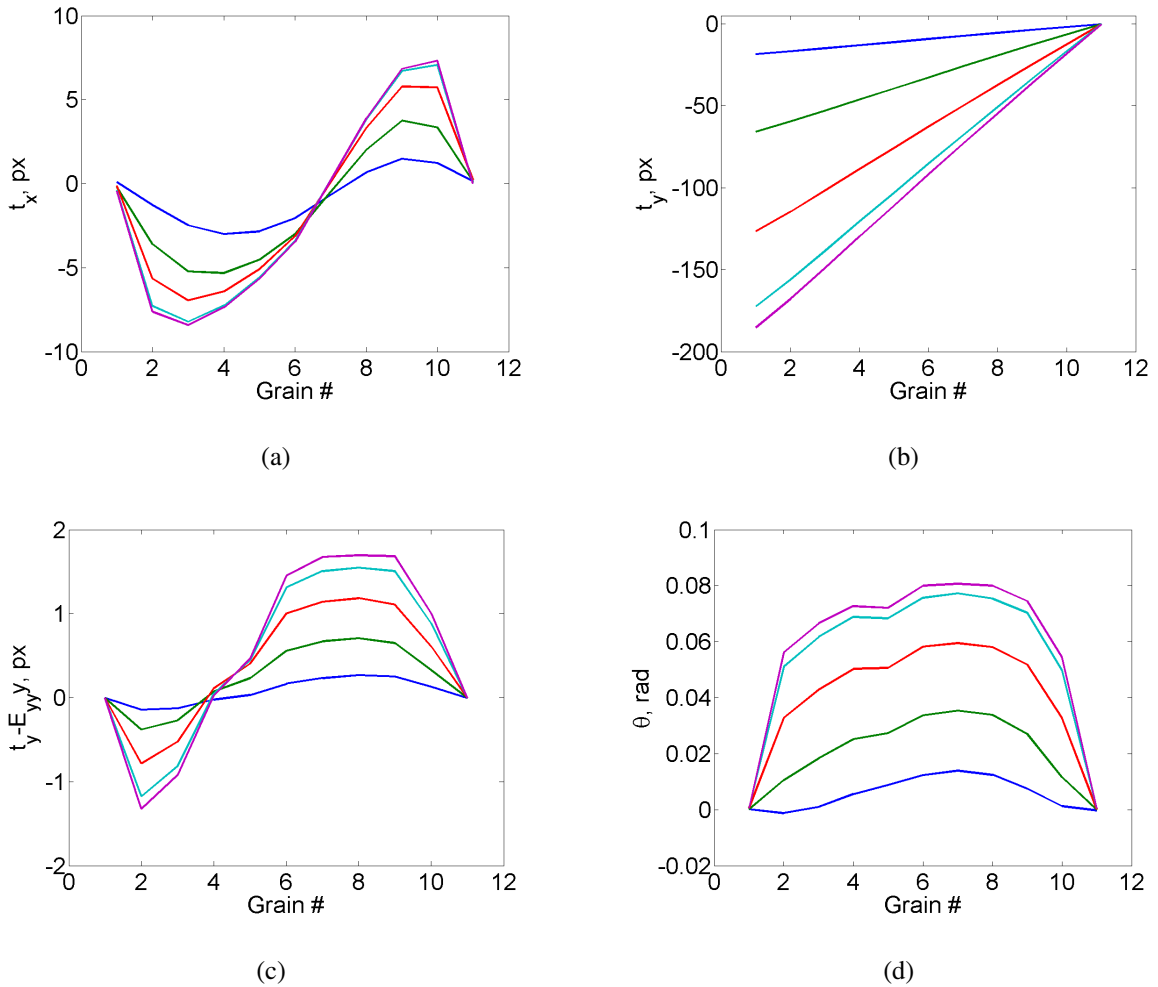


**Figure 24:** Change of the transverse translation (a), longitudinal translation (b), fluctuations of longitudinal translation, and rotation (d) of the eleven grains for all analyzed images of the dotted surface (for line color, refer to Figure 20(a))

650 The analysis at the grain scale could also be performed by only following the displacement  
 651 of each dot center thanks to 4-element zones (Figure 25). The gray level residuals are very low,  
 652 which again validates the reported measurements. All the trends observed at the microscale are  
 653 again present in these last results.

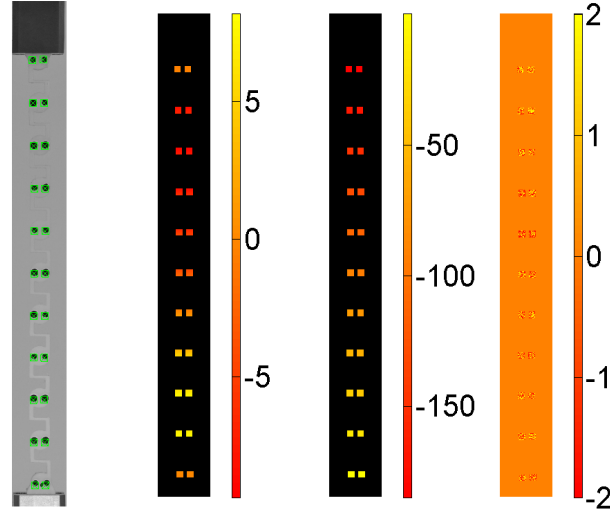


**Figure 25:** Mesh laid over the reference picture for the local analyses of the dotted surface (leftmost). Transverse displacement (expressed in px) field for the last analyzed picture (left). Corresponding longitudinal displacement (expressed in px) field (right) and gray level residual field (rightmost)

654

## 8. Appendix B: DIC Framework

Different parameterizations of the sought displacement field were considered (see Section 3.1) and are stated in a general form as

$$\mathbf{u}(\mathbf{x}, \{\mathbf{v}\}) = \sum_i \Phi_i(\mathbf{x}, v_i) \quad (1)$$

where  $v_i$  is the degree of freedom (DOF) associated with the  $i$ -th trial displacement field  $\Phi_i(\mathbf{x}, v_i)$ , and all DOFs are gathered in the column vector  $\{\mathbf{v}\}$ . In many cases, a linear dependence of the trial field with respect to the sought DOF may be assumed

$$\Phi_i(\mathbf{x}, v_i) = v_i \boldsymbol{\varphi}_i(\mathbf{x}) \quad (2)$$

with no summation over index  $i$ . This is for instance the case when seeking rigid body translations or using finite element discretizations of the displacement field. On the other hand, when large rigid body rotations are expected, then the corresponding displacement field  $\Phi_{RBR}$  is given as

$$\Phi_{RBR}(\mathbf{x}, \boldsymbol{\theta}) = [\mathbf{R}(\boldsymbol{\theta}) - \mathbf{I}]\mathbf{x} \quad (3)$$

655 where  $[\mathbf{R}(\theta)]$  is the rotation matrix, which non-linearly depends upon the angle  $\theta$ , and  $[\mathbf{I}]$  the  
 656 identity matrix.

Let us introduce the kinematic sensitivities, namely, the partial derivatives of the trial displacement field  $\Phi_i$  with respect to the corresponding DOF  $v_i$

$$\mathbf{s}_i(\mathbf{x}, v_i) = \frac{\partial \Phi_i}{\partial v_i}(\mathbf{x}, v_i) \quad (4)$$

657 If the trial displacement field  $\Phi_i$  is linearly dependent on its DOF  $v_i$ , then  $\mathbf{s}_i \equiv \boldsymbol{\varphi}_i$ , otherwise

$$658 \mathbf{s}_{RBR}(\mathbf{x}, \theta) = \partial[\mathbf{R}(\theta)]/\partial\theta \mathbf{x}.$$

In the DIC analyses, the DOFs  $\{\mathbf{v}\}$  are the unknowns to be determined. To this end, the sum of squared gray level residuals over the considered region of interest (ROI)

$$\rho_c^2(\{\mathbf{v}\}) = \sum_{\text{ROI}} \rho^2(\mathbf{x}, \{\mathbf{v}\}) \quad (5)$$

is minimized with respect to  $\{\mathbf{v}\}$  (Hild and Roux, 2012). The pixel-wise gray level residual is given  
 as

$$\rho(\mathbf{x}, \{\mathbf{v}\}) = f(\mathbf{x}) - g(\mathbf{x} + \mathbf{u}(\mathbf{x}, \{\mathbf{v}\})) \quad (6)$$

659 where  $f$  represents the image in the reference configuration, and  $g$  the image in the deformed  
 660 configuration. The root mean square (RMS) residual computed over the ROI,  $\rho_c^2$ , defines the overall  
 661 registration quality associated with the selected kinematic basis (*i.e.*, a measure of how well it  
 662 reproduces the deformed configuration with respect to the reference).

The minimization of  $\rho_c^2$  is performed via Gauss-Newton iterations stated as follows

$$[\mathbf{H}_c]\{\partial\mathbf{v}\} = \{\mathbf{h}_c\} \quad (7)$$

where  $[\mathbf{H}_c]$  denotes the DIC Hessian

$$(H_c)_{jk} = \sum_{\text{ROI}} (\nabla \tilde{g}(\mathbf{x}) \cdot \mathbf{s}_j(\mathbf{x})) (\nabla \tilde{g}(\mathbf{x}) \cdot \mathbf{s}_k(\mathbf{x})) \quad (8)$$

$\{\mathbf{h}_c\}$  the DIC residual vector

$$(h_c)_j = \sum_{\text{ROI}} (f(\mathbf{x}) - \tilde{g}(\mathbf{x})) (\nabla \tilde{g}(\mathbf{x}) \cdot \mathbf{s}_j(\mathbf{x})) \quad (9)$$

663 and  $\{\delta\mathbf{v}\}$  the corrections to the current estimates  $\{\tilde{\mathbf{v}}\}$  of the unknown DOFs. The minimization  
 664 scheme thus consists in gradually correcting the successive estimates  $\{\tilde{\mathbf{v}}\}$  of the DOFs. After each  
 665 iteration, the image  $g$  corrected by the measured displacement field  $\tilde{\mathbf{u}}$ , namely,  $\tilde{g}(\mathbf{x}) = g(\mathbf{x} + \tilde{\mathbf{u}}(\mathbf{x}))$   
 666 is updated for any pixel  $\mathbf{x}$  belonging to the ROI.

667 Given the fact that one of the speckle patterns was very coarse (Figure 15), there is a need  
 668 for some additional interpolation in particular in areas with low contrast if fine meshes are to be  
 669 considered. One possible route is to use regularization strategies (Tikhonov and Arsenin, 1977). In  
 670 the present case, a mechanics-based formulation was selected (Réthoré et al., 2009; Tomičević et al.,  
 671 2013). Conversely, when the kinematic basis is sufficiently reduced (*e.g.*, mesoscale analyses),  
 672 regularization was not considered.

The previous DIC cost function  $\rho_c^2$  is thus penalized with a second term (Tikhonov and Arsenin,  
 1977), which is constructed by computing the norm of the nodal forces for Hencky elasticity (*i.e.*,  
 minimizing the equilibrium gap (Claire et al., 2004)) written in terms of the incremental displace-  
 ments  $\{\delta\mathbf{v}\}$  between two consecutive pictures (dell'Isola et al., 2019)

$$\rho_m^2(\{\mathbf{v}\}) = \{\delta\mathbf{v}\}^\top [\mathbf{K}]^\top [\mathbf{K}] \{\delta\mathbf{v}\} \quad (10)$$

The minimization of augmented residual square  $\rho_t^2 = \rho_c^2 + w_m \rho_m^2$  is performed via Gauss-Newton  
 iterations as follows

$$[\mathbf{H}_{cm}] \{\delta\mathbf{v}\} = \{\mathbf{h}_c\} - w_m [\mathbf{K}]^\top [\mathbf{K}] \{\delta\tilde{\mathbf{v}}\} \quad (11)$$

with

$$[\mathbf{H}_{cm}] = [\mathbf{H}_c] + w_m [\mathbf{K}]^\top [\mathbf{K}] \quad (12)$$

673 where  $\{\delta\tilde{\mathbf{v}}\}$  denotes the current estimate of the incremental DOFs, and  $[\mathbf{K}]$  the stiffness matrix  
 674 associated with the chosen discretization. The weight  $w_m$  multiplying the second cost function is  
 675 proportional to a (regularization) length  $\ell_{reg}$  raised to the power 4 (Réthoré et al., 2009; Tomičević  
 676 et al., 2013). This length defines the physical size of the zone over which Hencky elasticity is

677 assumed to apply. In the present case, this length should be compatible with the coarseness of the  
678 speckle pattern (Figure 15) and with the fact that the underlying hypothesis of Hencky elasticity  
679 was (at least partially) satisfied. Consequently, rather large regularization lengths were selected in  
680 the present cases.

681 With the selected regularization strategy (Tomičević et al., 2013), the weight  $w_m$  is independent  
682 of the Young's modulus (provided it is positive). There is therefore no need for specifying it.  
683 Conversely, the stiffness matrix  $[\mathbf{K}]$  is nonlinearly related to the Poisson's ratio of the medium. A  
684 value of  $\nu = 0.35$  was selected, which is that of the durable resin utilized herein.